- Living on the edge: Response of <u>Late Cretaceous</u> rudist bivalves (Hippuritida) to hot and highly seasonal climate in the low-latitude Saiwan site, Oman
- Niels J. de Winter<sup>1,2</sup>, Najat al Fudhaili<sup>3</sup>, Iris Arndt<sup>4</sup>, Philippe Claeys<sup>2</sup>, René Fraaije<sup>5</sup>, Steven Goderis<sup>2</sup>, John
   Jagt<sup>6</sup>, Matthias López Correa<sup>7</sup>, Axel Munnecke<sup>7</sup>, Jarosław Stolarski<sup>8</sup>, Martin Ziegler<sup>9</sup>

#### Affiliations

- 1. Department of Earth Sciences, Vrije Universiteit Amsterdam, the Netherlands
- 2. Archaeology, Environmental Changes and Geo-Chemistry, Vrije Universiteit Brussel, Belgium
- 3. Industrial Innovation Academy LLC, Muscat, Oman
- 4. AG Geology and Paleoenvironmental research, Institut für Geowissenschaften, Goethe Universität
   Frankfurt, Germany
  - 5. Oertijdmuseum Boxtel, the Netherlands
    - 6. Natuurhistorisch Museum Maastricht, the Netherlands
    - 7. GeoZentrum Nordbayern, Friedrich-Alexander Universität, Erlangen, Germany
    - 8. Department of Environmental Paleontology, Institute of Paleobiology, Polish Academy of Science, Warsaw, Poland
    - 9. Department of Earth Sciences, Utrecht University, the Netherlands
- 19 Corresponding author: Niels J. de Winter (n.j.de.winter@vu.nl)

## Abstract

Earth's climate history serves as a natural laboratory for testing the effect of warm climates on the biosphere. The Cretaceous period featured a prolonged greenhouse climate characterized by higher-than-modern atmospheric  $CO_2$  concentrations and mostly ice-free poles. In such a climate, shallow seas in low latitudes probably became very hot, especially during the summers. At the same time, life seems to have thrived there in reef-like ecosystems built by rudists, an extinct group of bivalve molluscs. To test the seasonal temperature variability in this greenhouse period, and whether temperature extremes exceed the maximum tolerable temperatures of modern marine molluscs, we discuss a detailed sclerochronological (incrementally sampled) dataset of seasonal scale variability in shell chemistry from fossil rudist (*Torreites sanchezi* and *Vaccinites vesiculosus*) and oyster (*Oscillopha figari*) shells from the late Campanian (75-million-year-old) low latitude (3°S paleolatitude) Saiwan site in present-day Oman. We combine trace element data and microscopy to screen fossil shells for diagenesis, before sampling well-preserved sections of a *Torreites sanchezi* rudist specimen for clumped isotope analysis. Based on this specimen alone, we identify a strong seasonal variability in temperature of  $19.2 \pm 3.8^{\circ}$ C to  $44.2 \pm 4.0^{\circ}$ C in the seawater at the Saiwan site. The oxygen isotopic composition of the seawater ( $\delta^{18}O_{sw}$ ) varied from  $4.62 \pm 0.86 \%$  VSMOW in winter to  $+0.86 \pm 1.6 \%$  VSMOW in summer.

We use this information in combination with age modelling to infer temperature seasonality from incrementally sampled oxygen isotope profiles sourced from the literature, sampling multiple shells and species in the assemblage. We find that, on average, the Saiwan seawater experienced strong seasonal

fluctuations in monthly temperature (18.7 ± 3.8 to 42.6 ± 4.0 °C seasonal range) and water isotopic composition (-4.33 ± 0.86 to 0.59 ± 1.03 %vSMOW). The latter would strongly bias the interpretation of stable oxygen isotopes in shell carbonate without independent control on either temperature or seawater composition.

Combining our seasonal temperature estimates with shell chronologies based on seasonal cyclicity in stable isotope records and daily variability in trace element data, we show that *T. sanchezi* rudists record temperatures during the hottest periods of the year as well as during the winters, which were characterized by cooler temperatures and enhanced influx of freshwater. Both *O. figari* and *V. vesiculosus* plausibly stopped growing during these seasonal extremes. This study aims to demonstrate how high-resolution geochemical records through fossil mollusc shells can shed light on the variability in past warm ecosystems and open the discussion about the limits of life in the shallow marine realm during greenhouse climates. Future work should apply the clumped isotope paleothermometer on incrementally sampled bio-archives to explore the upper-temperature limits experienced by calcifiers in different environments throughout geological history.

## 1. Introduction

54

55

56 57

58 59

60

61

62

63

64 65

66 67

68

69 70

71

72

73

74

75

76

77

78

79

80

81

82

83

84

85

86

87

88

89

90

91

92

93

94

95

96

Ongoing anthropogenic global changes, including greenhouse gas emissions and land use changes, are projected to increase global mean annual temperatures by multiple degrees with respect to pre-industrial conditions, while at the same time causing severe biodiversity loss (IPCC, 2023; World Wildlife Fund, 2020). These crises are intricately linked, but assessing the effect of climate change on biodiversity loss requires information on the response of biodiversity to climate extremes under various (paleo)climate scenarios. The geological record provides a rich source of such information in the form of fossil bio-archives that record climate and environmental change on the scale of days to decades, while testifying to biodiversity by their presence in the rock record (Huyghe et al., 2012; Ivany, 2012; Schmitt et al., 2022). Past ecosystems thus serve as natural experiments for testing the limits of life during periods of global change or in exceptionally warm periods (Cermeño et al., 2022; de Winter et al., 2017; Jones et al., 2022).

Examples of hot periods that may reveal ecosystems' functioning under high-temperature climate scenarios include the early Triassic super greenhouse (Sun et al., 2012), the Mid-Cretaceous Climate Optimum (Jones et al., 2022) or the Eocene hothouse period (de Winter et al., 2020; Evans et al., 2013). Milder, yet still warmer than present-day, scenarios of interest include the Late Cretaceous ( de Winter et al., 2020; O'Hora et al., 2022; Petersen et al., 2016a), the Miocene Climatic Optimum (Batenburg et al., 2011; Harzhauser et al., 2011) and the Pliocene Warm Period (de Winter et al., 2024; Dowsett et al., 2013; Wichern et al., 2023). While these periods feature long-term, equilibrated climate states instead of fast, transient climate change events (like modern anthropogenic warming), they can yield useful insights into the long-term response of the climate system and biosphere to prolonged radiative forcing (Burke et al., 2018). For example, some of these past environments, most notably shallow marine ecosystems, are thought to have reached temperatures exceeding the temperature range of modern equivalent ecosystems (de Winter et al., 2020; Huang et al., 2017; Jones et al., 2022). and These temperatures probably exceeded the maximum temperature tolerance at which modern shallow marine species can complete their life cycle, which is typically estimated in the order of 38-42°C (Compton et al., 2007). (Compton et al., 2007; de Winter et al., 2020; Huang et al., 2017; Jones et al., 2022). Conditions that exceed this threshold (>38°C) are considered high-temperature conditions for shallow marine calcifiers to live in.

A striking conundrum arises in the Late Cretaceous Tethys Ocean margins, which were inhabited by large rudist bivalves biostromes (Skelton, 2018) despite apparently high water temperatures. The atmospheric CO<sub>2</sub> concentrations during the Campanian (83.6 - 72.1 Ma (Gradstein et al., 2020)) were ~600 ppmV (roughly 2x pre-industrial concentrations (Wang et al., 2014)), resulting in low- to mid-latitude mean annual sea surface temperatures (SST) of 20-25°C (O'Brien et al., 2017), roughly 5-10°C warmer than the current global mean annual temperature. In low-latitude Tethyan margins, mean annual temperatures likely exceeded 30°C (Steuber et al., 2005), with summer temperatures estimated above 40°C in some localities (de Winter et al., 2017, 2020; Steuber, 1999). A big caveat of these estimates is that they rely on the temperature dependence of stable oxygen isotope analyses and are contingent on assumptions of (seasonally) constant stable oxygen isotope composition of Tethyan seawater, which is known to have fluctuated over time (Price et al., 2020; Walliser and Schöne, 2020). If correct, such temperatures exceed the temperature threshold of 38°C mentioned above and are at or above the lethal thermal limits for modern marine invertebrates (typically 42-50°C; (Clarke, 2014; Compton et al., 2007)). These temperatures approach the thermal threshold above which critical macromolecules such as ATP, proteins, and enzymes used by non-extremophile organisms denature (>50°C) (Clarke, 2014; Tehei et al., 2005; Tehei and Zaccai, 2007), hampering key metabolic functions. Yet, despite these apparent temperature extremes,

Formatted: English (United States)

Field Code Changed

abundant and diverse fossil shallow marine ecosystems suggest that rudists thrived in these environments (Gili and Götz, 2018; Ross and Skelton, 1993). This raises the question of whether these paleotemperature reconstructions are accurate, and if so, whether these ancient molluscs were somehow adapted to grow their shells at these extreme temperatures.

In an attempt to resolve this thermal tolerance conundrum, we investigate the growth and chemical composition of two species of rudist bivalve (Torreites sanchezi and Vaccinites vesiculosis) and one oyster species (Oscillopha figari) from the low-latitude Tethyan site in the Saiwan area in east-central Oman (Kennedy et al., 2000; Schumann, 1995). Our analysis combines new sclerochemical data, including clumped isotope analyses, with existing stable oxygen isotope datasets from the literature. We aim to test how the growth of these animals responded responds to seasonal temperature extremes. To obtain accurate seasonal temperature reconstructions, which are independent from the Tethyan seawater composition and ex vivo diagenetic alteration, we bring together trace element, stable oxygen isotope, and clumped isotope information that are independent of the Tethyan seawater composition and ex vivo diagenetic alteration, we combine information on trace elements, stable oxygen isotopes, and clumped isotopes. Using a new clumped isotope dataset, we first demonstrate that T. sanchezi records temperatures in their shells that significantly exceed the threshold at which modern marine molluscs thrive. We then build on our clumped isotope dataset to test how shell growth was influenced by these seasonal temperature extremes in this paleoenvironment by combining our results with stable oxygen isotope records from the literature, augmented with new shell chronologies and growth models. We contrast our seasonality and growth rate reconstructions with data on the thermal ranges of modern bivalves to compare the tolerance of biostrome-building rudists in the Late Cretaceous with modern species. Ultimately, this case study will open the discussion of the ability of marine life to adapt to hot climates and provide lessons for the interaction between climate change and marine biodiversity.

Formatted: Font: Italic

97

98

99

100

101

102

103

104

105

106

107

108

109

110

111

112

113

114

115

116

117118

## 2. Materials and Methods

## 121 2.1 Fossil mollusc specimens

The mollusc shells utilized in this work originate from the Samhan Formation in the Saiwan area of Oman in the Huqf desert (30°39 N, 57°31 E; see Figure 1A). The biostromes in this locality were dated as late Campanian (~75 Ma) based on ammonite biostratigraphy by {Kennedy et al., (2000). The paleolatitude of the site at 75 Ma was 3°S according to reconstructions following Paleolatitude.org (van Hinsbergen et al., 2015) based on the paleomagnetic reference frame by {Vaes et al., (2023). The locality was described by (Schumann, 1995) as exposing *Vaccinites*-dominated rudist biostromes in which rudist bivalves are preserved in their life position (see also Figure 1B-C). The *V. vesiculosus* and *T. sanchezi* specimens used and reused in this study originate from Unit IV in profile 1 of {Schumann, (1995), which is equivalent to unit 2 in (Philip and Platel, 1995). The thick-shelled *O. figari* oysters were collected in the marly layer just above the biostrome (see also Figure 1B-C and de Winter et al. (2017)).

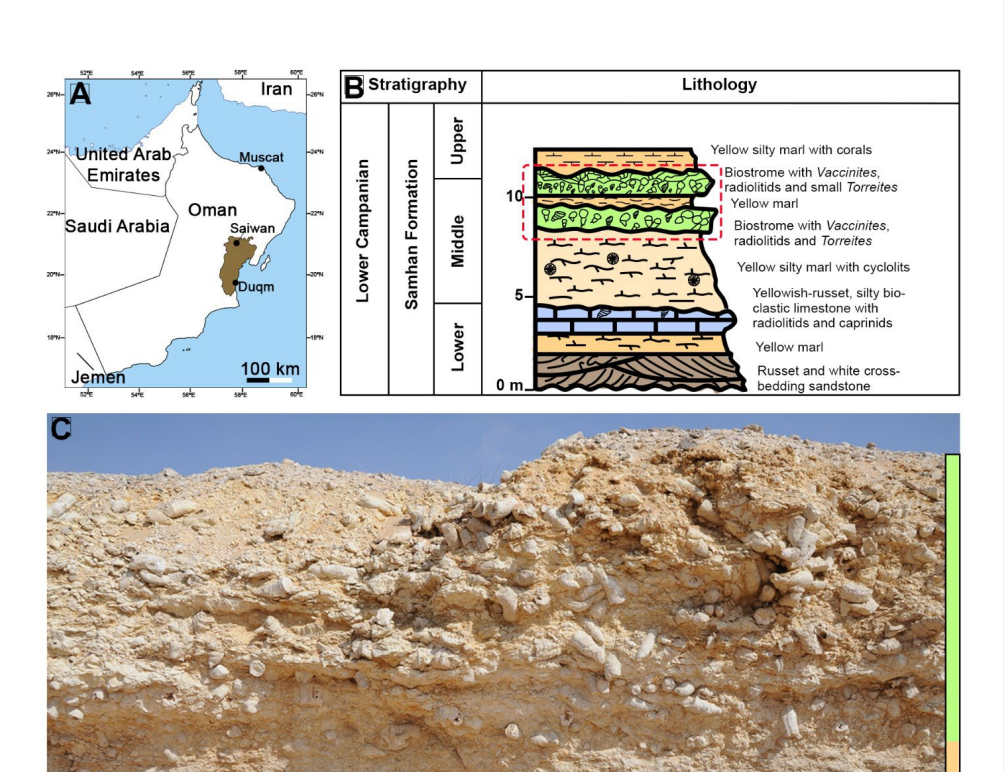


Figure 1: Showing (A) AmMap of the geographical location of the Late Campanian Samhan fromation in the Saiwan area in the central part of the Sultanate of Oman. (B) Lithostratigraphic column showing the stratigraphic context of the characteristic members of the Samhan Formation. The red dashed box indicates the stratigraphic location of the outcrop pictured in (C). The marly layer containing O. figari referred to in the text is the brown layer in between the two green members in the dashed red box. (C) Outcrop showing the two Vaccinites-dominated biostromes, the lower of which contained the T. sanchezi and V. vesiculosus specimens investigated in this study (indicated by the schematic images of the species). The O. figari specimen was collected in the marly layer just above the biostrome containing the other specimens (indicated by the schematic image), between the two green units in (B). Panel (B) was modified after (Philip and Platel, 1995).

All specimens described in this study were sampled in <u>longitudinal</u> cross\_sections through the axis of maximum growth using a combination of hand drilling and computer-assisted microdrilling using slow-

rotating tungsten carbide dental drills. **Table 1** gives an overview of the data used in this study, its temporal resolution and the source of datasets in cases where they have been reused from the literature. *V. vesiculosus* specimen "**B6**", *T. sanchezi* specimen "**B10**" and *O. figari* specimen "**B11**" were described in ( de Winter et al., 2017) and stable isotope ( $\delta^{18}$ O and  $\delta^{13}$ C) and trace element (Mg, Sr, Ca, Mn, Fe) data presented in that study are used here. Specimen **B10** was also subject of a study by (de Winter et al., 2020), in which more detailed, daily scale trace element measurements (Mg/Ca, Sr/Ca, Mg/Li and Sr/Li) were presented and discussed. Stable isotope ( $\delta^{18}$ O and  $\delta^{13}$ C) data from *T. sanchezi* specimens "**H576**", "**H579**" and "**H585**" was previously reported in (Steuber, 1999). Of these, specimen **H579** was sampled in 5 parallel sections ("**H579A-E**").

Specimen	Species	Proxy	# data points	Resolution	Source						
		$\delta^{18}O$	306	~2 weeks	(de Winter et al., 2017)						
В6		$\delta^{13}C$	306	~2 weeks	(de Winter et al., 2017)						
	V.	Mg/Ca	735	~1 week	(de Winter et al., 2017)						
	vesiculosus	Sr/Ca	735	~1 week	(de Winter et al., 2017)						
		Mn	735	~1 week	(de Winter et al., 2017)						
		Fe	735	~1 week	(de Winter et al., 2017)						
		δ <sup>18</sup> O	310	~2 weeks	(de Winter et al., 2017, 2020)						
		$\delta^{13}C$	310	~2 weeks	(de Winter et al., 2017, 2020)						
		Mg/Ca	12443	~0.5h	(de Winter et al., 2020)						
		Sr/Ca	12535	~0.5h	(de Winter et al., 2020)						
D4.0	- , .	Mg/Li	12167	~0.5h	(de Winter et al., 2020)						
B10	T. sanchezi	Sr/Li	12322	~0.5h	(de Winter et al., 2020)						
		Mg/Ca	4353	1-5h	(de Winter et al., 2017)						
		Sr/Ca	4361	1-5h	(de Winter et al., 2017)						
		Mn	4043	1-5h	(de Winter et al., 2017)						
		Fe	3972	1-5h	(de Winter et al., 2017)						
H576	T. sanchezi	$\delta^{18}O$	98	~3 weeks	(Steuber, 1999)						
		$\delta^{13}C$	98	~3 weeks	(Steuber, 1999)						
	T. sanchezi		288								
		$\delta^{18}O$	(116 + 46 +	~3 weeks	(Steuber, 1999)						
H579			47 + 35 + 44)								
(5 profiles:			288		(Steuber, 1999)						
A-E)		$\delta^{13}C$	(116 + 46 +	~3 weeks							
			47 + 35 + 44)								
H585	T samahari	δ <sup>18</sup> O	132	~1 month	(Steuber, 1999)						
нэөэ	T. sanchezi	$\delta^{13}C$	132	~1 month	(Steuber, 1999)						
		δ <sup>18</sup> Ο	221	1 2 days	This study (BSc thesis N. al-						
		80	231	1-2 days	Fudhaili)						
HU-027	T. sanchezi	δ <sup>13</sup> C	231	1-2 days	This study (BSc thesis N. al-						
				,	Fudhaili)						
		Δ <sub>47</sub>	86	Seasonal	This study						
		Si & Ca	map	Spatial map	This study						
		δ18Ο	90	~3 weeks	(de Winter et al., 2017)						
		δ <sup>13</sup> C	90	~3 weeks	(de Winter et al., 2017)						
B11	O. figari	Mg/Ca	402	~3-7 days	(de Winter et al., 2017)						
_	- 7.5	Sr/Ca	402	~3-7 days	(de Winter et al., 2017)						
		Mn	402	~3-7 days	(de Winter et al., 2017)						
		Fe	367	~3-7 days	(de Winter et al., 2017)						

Specimens **H576**, **H579** and **H585** were subject to detailed diagenetic screening in (Steuber, 1999) and the preservation of specimens **B6**, **B10** and **B11** was tested in (de Winter et al., 2017, 2020; de Winter and Claeys, 2016). These previous studies concluded, based on a combination of scanning electron microscopy, cathodoluminescence microscopy and trace element analysis, that there was no <u>detectible\_detectable</u> recrystallization in the areas of the shells sampled for geochemical analysis and that the low-magnesium

calcite outer shell layer of these rudists preserves the original shell composition deposited during the lifetime of the animal. For the purpose of this study, additional screening based on high-resolution trace element analyses (Mg/Ca, Sr/Ca, Mn and Fe) will be discussed for specimens **B6**, **B10** and **B11**, one specimen for each of the three studied species (see **sections 3.2** and **4.1**). The newly sampled specimen **HU-027** was subject to detailed microscopic scrutiny using a combination of reflected light, cross-polarized light, scanning electron microscopy and energy dispersive X-ray spectroscopy (EDS) and micro-Raman spectroscopy to characterize original shell texture preservation and detect diagenetic alteration (**Figure 2C-F**).

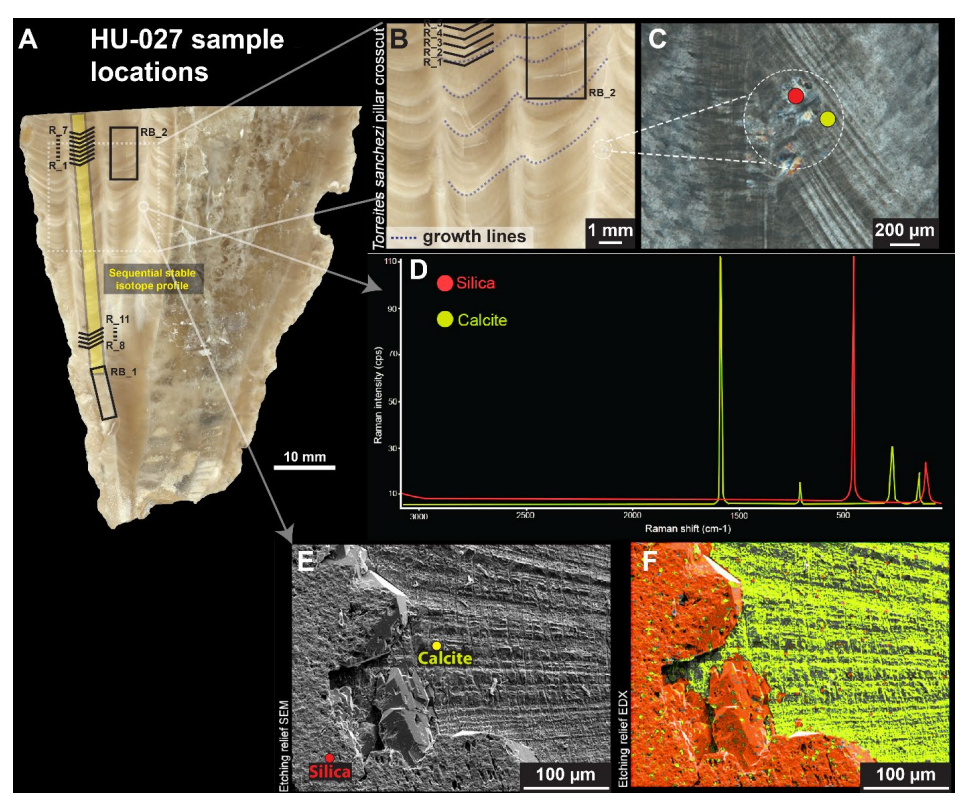


Figure 2: A) High-resolution colour scan of a  $\frac{cross\_section}{cross\_section}$  through T. sanchezi specimen HU-027 with the location of samples for  $\delta^{18}O$ ,  $\delta^{13}C$  (yellow rectangle) and clumped isotope analysis ( $\frac{inblack}{inblack}$  text and lines-red). B) Zoomed-in insert showing fine lamination in columns through HU-027, the location of samples RB\_2 and R\_1 - R\_5, and examples of isochronous growth lines (dashed lines) that link the timing of growth between pillars in the cross\\_section. C) Cross-polarized light image of the edge of a shell column showing locations for characterizing diagenetic (silicified) and pristine areas in the shell. D) Raman spectra of pristine calcite ( $\frac{cross\_section}{cross\_section}$ ) and silicified (red) areas in the shell of HU-027. E) Scanning Electron Microscopy fore scatter image of the area of interest highlighted in B, showing original calcite shell structures (right) and silicified areas of the shell (left). F) Energy-dispersive X-ray spectroscopy (EDS)

- image of the same area shown in **E** showing the silicon (red<u>tellowred</u>) and calcium (greenyellow) composition on a micrometre scale.
- 191 2.2 Chemical data
- 192 2.2.1 X-ray fluorescence
- To test the preservation of shells of the specimens **B6**, **B10** and **B11**, trace element concentrations were
- analysed *in situ* using a Bruker M4 Tornado (Bruker nano GmbH) micro-X-ray fluorescence (µXRF) scanner
- 195 (see de Winter and Claeys (2016)). The M4 is equipped with a Rh-anode X-ray source, which was operated
- at maximum energy settings (50 kV, 600  $\mu$ A) without an X-ray filter, and X-rays were focused on a 25  $\mu$ m
- 197 circular spot (calibrated for Mo-kα radiation) on the flat sample surface. Fluorescent X-rays were detected
- 198 using two silicon drift detectors for maximum count rates.
- 199 Cross\_-sections of the entire specimens were first mapped to determine the best preserved sampling
- 200 localities based on Mn and Fe concentrations (see de Winter et al. (2017)). This μXRF mapping was carried
- 201 out by moving the X-ray beam along the sample surface in a raster pattern while continuously collecting
- 202 XRF spectra. Since this mapping mode allows to only collect fluorescent X-rays for ~1 millisecond for each
- 203 25 μm-wide pixel, XRF spectra of individual pixels cannot be quantified. Instead, maps were quantified as
- a whole by integrating the area under XRF peaks for all pixels, producing false-colour images of semi-
- 205 quantitative trace element abundance across the entire specimen (see de Winter et al. (2017)).
- 206 Quantitative XRF profiles were gathered in growth direction on cross\_-sections through the shells by
- 207 analysing point-by-point line scans (see Vansteenberge et al., (2020). This point-by-point analysis allows
- 208 the X-ray beam to dwell on a single spot for 60 seconds, allowing the detectors to gather enough XRF
- counts for a quantifiable XRF spectrum (de Winter et al., 2017). XRF data were quantified through a combination of peak deconvolution and fundamental parameter quantification in the Bruker Esprit
- combination of peak deconvolution and fundamental parameter quantification in the Bruker Esprit software (Bruker nano GmbH), calibrated using the matrix-matched carbonate reference material BAS-
- 212 CRM393 (Bureau of Analyzed Samples, Middlesbrough, UK). Quantified trace element concentrations
- were subsequently calibrated based on a set of 10 matrix-matched carbonate reference materials (see
- 214 (Vellekoop et al., 2022) to obtain reproducible trace element concentrations. The XRF maps and line scans
- were used to demonstrate the preservation of the original calcium carbonate in specimens **B6**, **B10** and
- 216 B11. Full XRF datasets for all analysed specimens are provided in Supplement S1 in the accompanying
- 217 Zenodo repository (<a href="https://doi.org/10.5281/zenodo.12567712">https://doi.org/10.5281/zenodo.12567712</a>).
- 2.2.2 Laser Ablation Inductively Coupled Plasma Mass Spectrometry
- 219 High-resolution Laser Ablation-Inductively Coupled Plasma Mass Spectrometry (LA-ICP-MS) profiles of Li,
- 220 Mg, Sr, Ca, Mn and Fe concentrations through T. sanchezi specimen B10 were reused from ( de Winter et
- al., 2020). These profiles were measured using an Analyte G2 ArF\*excimer-based laser ablation system
- 222 (Teledyne Photon Machines, Bozeman, USA) coupled to an Agilent 7900 (for LA-ICP-MS; Agilent, Santa
- 223 Clara, USA) quadrupole-based ICP-MS unit. The laser was focused on a round 10 μm spot on the sample
- 224 surface and translated continuously in line scanning mode to gather sub-daily resolved data along the
- 225 entire shell height. LA-ICP-MS results were calibrated using repeated measurements of United States
- 226 Geological Survey (USGS) BCR-2G, USGS BHVO-2G, USGS GSD-1G, and USGS-GSE-1G $_{\tiny L}$  and National
- 227 Institute of Standards and Technology SRM610 and National Institute of Standards and Technology

SRM612 certified natural and synthetic glass reference materials. All LA-ICP-MS concentration data are provided in **Supplement S1** in the Zenodo repository.

#### 230 2.2.3 Isotope Ratio Mass Spectrometry

231

232

233 234

235

236

237

238

239

240

241242

243

244

245

246

247248

249

250

251

252

253

254

255

256

257

258

259

260

261

262

263

264

265

266

267

Stable carbon ( $\delta^{13}$ C) and oxygen ( $\delta^{18}$ O) values from specimens **B6**, **B10**, **B11**, **H576**, **H579** and **H585** were reused from (de Winter et al., 2017) and (Steuber, 1999). This dataset was augmented by new sequentially sampled  $\delta^{13}$ C and  $\delta^{18}$ O measurements along the central pillar through specimen **HU-027** (see **Figure 2**). All  $\delta^{13}$ C and  $\delta^{18}$ O data were obtained by analysing carbonate powders sampled in cross\_sections through the specimens using an Isotope Ratio Mass Spectrometer (IRMS) coupled to a carbonate preparation device. The stable isotope analyses for the incremental samples in **HU-027**, specifically, were analysed by a Thermo DELTA V+ IRMS coupled to a Gasbench carbonate preparation device. During sampling, care was taken to avoid areas in the shell characterized by elevated Mn and Fe concentrations (see trace element results in **section 3.2** and (de Winter et al., 2017)) and microscopic signs of diagenetic alteration (see **Figure 2**). Standard deviations of uncertainty on  $\delta^{13}$ C and  $\delta^{18}$ O values produced using this technique are 0.05 % and 0.10 %, respectively. An overview of the  $\delta^{13}$ C and  $\delta^{18}$ O records through all IRMS profiles is provided in **Supplement S2** in the Zenodo repository.

Representative samples from two parallel central pillars of specimen HU-027 were sampled for clumped isotope analysis (see Figure 2). During sampling, care was taken to avoid the diagenetically altered sections of the shell (Figure 2C-F). Two areas in HU-027 were drilled for bulk clumped isotope analysis ("RB\_1" and "RB\_2"; Figure 2A; see section 2.1), after which samples were drilled from transects in growth direction along one of the pillars exposed in the shell (Figure 2A). A total of 94 small (70-95 μg) aliquots of calcite powder were reacted with anhydrous (103%) phosphoric acid in a Kiel IV carbonate device. The resulting CO<sub>2</sub> was cryogenically purified and cleaned using a PoraPak Q trap kept at -40 °C (Petersen et al., 2016b) before being led into a MAT253 or MAT253 PLUS IRMS via a Dual Inlet system. Intensities on masses 44-49 of the CO<sub>2</sub> samples were measured using the Long Integration Dual Inlet mode (Müller et al., 2017) with 400 s integration time against a clean CO<sub>2</sub> working gas ( $\delta^{13}$ C = -2.82 %;  $\delta^{18}$ O = -4.67 %), corrected for the pressure baseline (He et al., 2012). Clumped isotope values ( $\Delta_{47}$ ) were brought into the Intercarb Carbon Dioxide Equilibrium Scale (I-CDES; (Bernasconi et al., 2021) using the three ETH standards (ETH-1, ETH-2 and ETH-3) and their accepted values (Bernasconi et al., 2018). Throughout this procedure, samples were corrected with standards whose signal intensities on the mass 44 cup deviated from the intensities of the samples by less than 1 V to prevent any intensity-based offset in the clumped isotope values to bias the result. For samples for which less than 5 intensity-matched standards were available for this correction, the  $\Delta_{47}$  value was not considered in the rest of the analysis. The complete analytical system was monitored regarding performance with two independent standards (IAEA-C2, N = 49, and Merck, N = 48), which were treated as samples throughout the measurement procedure. The standard deviations of  $\Delta_{47}$  values of these check standards were 0.053‰ for IAEA-C2 and 0.039 ‰ for Merck. The reproducibility standard deviations of  $\delta^{13}$ C and  $\delta^{18}$ O for IAEA-C2 were 0.05 ‰ and 0.09 ‰ respectively and for Merck the reproducibility standard deviations were 0.09 % and 0.13 % for  $\delta^{13}$ C and  $\delta^{18}$ O respectively. Results of clumped and associated stable isotope data are reported in Supplement S2 in the Zenodo repository. A summary of the  $\delta^{13}$ C,  $\delta^{18}$ O and  $\Delta_{47}$  values organized by the four regions of **HU-027** that were sampled (see Figure 2) is presented in Table 2.

**Table 2**: Statistics of carbon, oxygen and clumped isotope results organized per sampled region in specimen **HU-027**.

Sampled region:	F	R_01-R_0	7	F	R_08-R_1	1		RB_1		RB_2					
Proxy:	Δ <sub>47</sub> (‰ I-CDES)	$\begin{array}{c} \delta^{18}O \\ (\text{‰ VPDB}) \end{array}$	$\begin{array}{c} \delta^{13} \text{C} \\ \text{($\%$ VPDB)} \end{array}$	Δ <sub>47</sub> (‰ I-CDES)	$\begin{array}{c} \delta^{18}O \\ (\text{‰ VPDB}) \end{array}$	$\begin{array}{c} \delta^{13} \text{C} \\ \text{($\%$ VPDB)} \end{array}$	Δ <sub>47</sub> (‰ I-CDES)	$\begin{array}{c} \delta^{18}O \\ (\text{‰ VPDB}) \end{array}$	$\begin{array}{c} \delta^{13} \text{C} \\ \text{($\%$ VPDB)} \end{array}$	Δ <sub>47</sub> (‰ I-CDES)	$\begin{array}{c} \delta^{18}O \\ (\text{\% VPDB}) \end{array}$	$\begin{array}{c} \delta^{13} \text{C} \\ \text{($\%$ VPDB)} \end{array}$			
N	29	35	35	16	20	20	27	27	27	14	14	14			
Median value	0.544	-6.12	0.66	0.560	-4.71	2.02	0.608	-5.81	1.37	0.569	-5.02	1.67			
Mean value	0.543	-6.13	0.73	0.560	-4.71	2.02	0.614	-5.80	1.37	0.577	-5.03	1.67			
Standard deviation	0.032	0.26	0.35	0.035	0.20	0.12	0.037	0.06	0.04	0.027	0.08	0.02			
Minimum	0.460	-6.75	-0.14	0.504	-5.22	1.76	0.557	-5.93	1.30	0.540	-5.28	1.60			
Maximum	0.589	-5.67	1.43	0.619	-4.42	2.28	0.697	-5.70	1.46	0.621	-4.97	1.70			

## 2.3 Modern bivalve occurrence and climate

To contrast the paleoclimate reconstructions from the above-mentioned multi-proxy dataset, we extracted data on the occurrences of bivalves in modern oceans from the Ocean Biodiversity Information System database (OBIS, 2020). We accessed the OBIS database through the "occurrences" function of the "robis" package (Provoost et al., 2022) and processed the occurrences in the open-source computational software package R (R Core Team, 2023). A total of 2199523 occurrences of taxa in the class of Bivalvia were extracted from the database, and their localities were categorized in bins of 2° by 2° based on their latitude and longitude.

Modern seasonal SST ranges across the world oceans were extracted from the Extended Reconstructed Sea Surface Temperature (ERSST) dataset from the National Oceanic and Atmospheric Administration (NOAA; (Huang et al., 2017)). We extracted monthly data from the years 1981 until 2010 on a 2° by 2° latitude and longitude grid from the ERSST dataset. We extracted the warmest and coldest monthly temperatures from the grid cells that contained reported occurrences of bivalves in the OBIS dataset. This resulted in a distribution of the warmest and coldest monthly temperatures across the living environment of modern bivalves.

# 2.4 Data processing

Our clumped isotope dataset on specimen **HU-027** yielded information about the seasonal spread in temperature and the water oxygen isotopic value ( $\delta^{18}O_w$ ) experienced by this specimen. We reconstructed these parameters from the  $\Delta_{47}$  and  $\delta^{18}O_c$  values of the shell carbonate following the clumped isotope-temperature relationship by (Daëron and Vermeesch, 2023) and the calcite  $\delta^{18}O_c$ - $\delta^{18}O_w$ -temperature relationship by (Kim and O'Neil, 1997). This dataset allowed us to characterize seasonal variability in climate in the Saiwan paleoenvironment. However, since the relatively short  $\delta^{18}O$  profile from **HU-027** did not allow age modelling and the clumped isotope dataset only sampled one specimen, we augmented the dataset from **HU-027** with  $\delta^{18}O$ ,  $\delta^{13}C$  and trace element data from other specimens (see section 2.2.3) in the same assemblage to study the relationship between temperature and growth rate in Saiwan. To achieve this, we carried out subsequent data processing steps outlined below.

To reconstruct shell growth rates of the molluscs and water temperatures in the Saiwan environment from chemical data measured in the shells, we carried out the following data processing steps (see also the flowchart in **Figure 3**):

- 1. We used concentrations of Mn and Fe and Mg/Ca and Sr/Ca ratios to screen for diagenetic recrystallization of parts of the shells, and remove chemical data from suspicious shell sections for further analysis.
- 2. We applied the ShellChron age model (de Winter, 2021) to produce internal shell chronologies based on seasonal cyclicity in  $\delta^{18}$ O and  $\delta^{13}$ C values through each shell profile.
- We applied the Daydacna age model (Arndt et al., 2023) to produce internal shell chronologies based on subdaily-scale trace element variability in specimen B10 to verify the result of the ShellChron algorithm.
- 4. We use a combination of oxygen isotope and clumped isotope data, grouped per location in specimen **HU-027** to reconstruct seasonal changes in temperature and  $\delta^{18}O_w$  in the Saiwan environment, and how they relate to the oxygen isotope variability in the shells.
- 5. We use the information about  $\delta^{18} O_w$  variability in the environment from clumped isotope data in **HU-027** to reconstruct seasonal temperature variability in the Saiwan ecosystem based on all  $\delta^{18} O$  profiles.
- 6. We combine seasonal-scale information about shell growth rates and temperatures to determine the maximum temperature at which the mollusc species mineralized their shell and to quantify the effect of temperature on shell growth rates in Saiwan.

Details on the diagenetic screening are discussed in **sections 3.2** and **4.1**. Assumptions and details regarding all data processing steps are explained below.

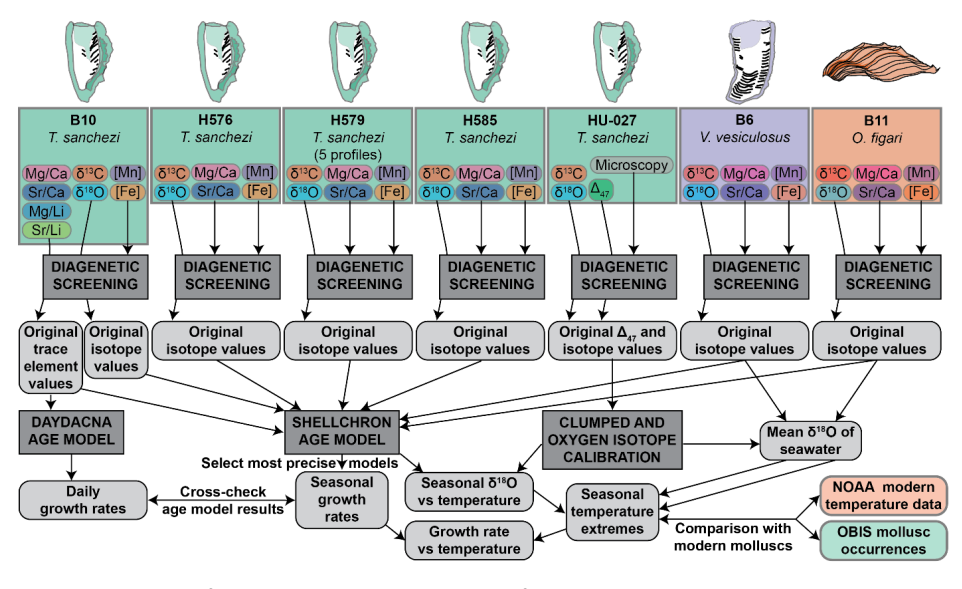


Figure 3: Flowchart of data processing steps carried out for this study.

2.4.1 Seasonal scale age models using ShellChron

Internal age models were created for all  $\delta^{18}O$  and  $\delta^{13}C$  profiles in all specimens except for **HU-027**, for which the  $\delta^{18}O$  and  $\delta^{13}C$  profile was too short to meet the criteria for applying the algorithm (see below),

as well as the Mg/Ca and Sr/Ca profiles in *T. sanchezi* specimen **B10** based on the growth rate modelling routine ShellChron (de Winter, 2021). ShellChron approximates the shape of the proxy curve from combinations of sinusoidal proxy and growth rate curves. The routine was adapted after the work by (Judd et al., 2017) to function in a sliding window algorithm to provide one age-distance model for the entire profile, preventing breaks and time jumps between growth years. ShellChron can approximate the internal chronology of any proxy-distance record using the following assumptions:

- 1. The proxy has a (quasi)\_periodic behaviour over the year. In other words: The proxy exhibits one maximum and one minimum per annual cycle.
- 2. The mineralization (or growth) rate of the archive over a year can be approximated by a (skewed) sinusoid, with one annual maximum and one minimum (which can be zero).
- 3. The proxy record contains at least 2 full annual cycles to allow for sufficient overlap between moving windows.

ShellChron estimates the uncertainties of age estimates per datapoint by comparing the results of overlapping windows on the proxy record during the sliding window approach which is applied in the model. Since the proxy-depth record in each window in the ShellChron model is estimated separately using a new combination of proxy and growth rate sinusoid, subsequent age estimates for the same distance value can have different, independent outcomes with respect to relative age estimate. In addition, ShellChron propagates the uncertainty on the distances and proxy values (if provided) using a Monte Carlo approach, resulting in a realistic estimate of the uncertainty on the age determination (de Winter, 2021). For each datapoint, the model thus produces a distribution of ages, from which an uncertainty on the relative age of each datapoint is obtained. These can in turn be averaged to gauge the overall precision of the model outcome. In addition, wide age distributions for the same datapoint are indicative of misidentifications of annual cycles in the  $\delta^{18}$ O profile, which cause bifurcations in the model outcome, increasing the spread in age outcomes. Therefore, the overall precision of the ShellChron outcome yields information about the certainty of age modelling and can be used as a benchmark for selecting the most reliable age-distance relationship in a shell. The shell height vs age relationships estimated using ShellChron for multiple proxy records ( $\delta^{18}$ O,  $\delta^{13}$ C and trace element ratios, if available) from each specimen except HU-027, including their uncertainties, are provided in Supplement S3 in the Zenodo repository. The age-distance relationships resulting from the most precise age model for each specimen were used to assign a time of the year to each stable isotope and trace element datapoint used in this study.

## 2.4.2 Sub-seasonal age model using Daydacna

For *T. sanchezi* specimen **B10**, from which subdaily-scale Mg/Ca, Mg/Li, Sr/Ca and Sr/Li data was-were available (de Winter et al., 2020), we applied the growth modelling routine Daydacna (Arndt et al., 2023) to verify the ShellChron results and enhance the resolution of the age model. Daydacna uses a wavelet transformation to detect daily rhythms in chemical profiles through mollusc shells and applies a user-guided peak identification routine to find age-depth relationships in the shell on a daily scale. We applied the Daydacna routine on subdaily scale Mg/Ca, Mg/Li, Sr/Ca and Sr/Li records one by one through specimen **B10** (see script in **Supplement S4** in the Zenodo repository). We compare the results of Daydacna with the results of ShellChron, which are based on annual cycles in  $\delta^{18}$ O and  $\delta^{13}$ C profiles and are therefore independent from the Daydacna results based on daily cycles in trace element ratios.

## 2.4.3 Monthly binning of isotope data

364 365

366

367

368

369

370

371

372

373

374

375

376

377

378

379

380

381

382

383

384

385

386

387 388

389

390

391

392

393

394

395

396

397

399

400

401

402

403

404

Stable isotope data from profiles through all specimens were cross-referenced with shell age results from ShellChron and Daydacna. Datapoints for which age modelling did not yield a conclusive age (e.g. stable isotope datapoints from locations in between data in trace element profiles) were dated by linear interpolation between surrounding samples for which dates were available. All chemical data were then binned into monthly time bins based on the age models. Monthly bins were assigned by dividing the year into 12 equal time segments, defining boundaries between months based on the day of the year. These monthly time bins were assigned 30 times for each specimen, shifting the boundaries between the months by 1 modelled day for each new assignment. The optimal monthly assignment was subsequently found by picking the option out of 30 in which the months with the highest and lowest mean  $\delta^{18}$ O value exhibited the highest difference. This age assignment is assumed to find the highest (least smoothed) seasonal variability in  $\delta^{18}$ O, while staying true to the sub-annual growth rate variability exhibited by the specimen as modelled by the ShellChron and Daydacna algorithms.

Note that this monthly binning assumes a total of 365 days in a year, while in reality the number of days per year during the Late Cretaceous was higher (de Winter et al., 2020). In addition, it is possible that growth stops occurgrowth stops may occur which prevent the mollusc from recording one or more days during periods of stress (Jones, 1983), even though no clear signs of these were directly observed in our specimens. However, this difference does not influence the monthly binning since 12 equal parts of the year were considered and the number of days per year assumed in the ShellChron and Daydacna models was also set to 365.

## 2.4.4 Combining clumped isotope and $\delta^{18}$ O data

To overcome the lack of precise intra-shell age control in HU-027 and place the clumped isotope results in a seasonal context, we grouped the  $\Delta_{47}$  and carbonate  $\delta^{18}$ O ( $\delta^{18}$ O<sub>c</sub>) data from specimen **HU-027** in four bins according to their sampling location (see Figure 2 and Table 2). This resulted in a seasonal spread of  $\Delta_{47}$ ,  $\delta^{18}O_c$  and  $\delta^{13}C$  values which allowed us to quantify the relationship between  $\delta^{18}O_c$  and  $\Delta_{47}$  (and therefore temperature and  $\delta^{18}O_w$ ) in the Saiwan environment.

To verify whether our choice of sampling locations for clumped isotope analysis in specimen HU-027 sampled the full seasonal spread in (clumped) isotopic values, we applied a clustering routine to the carbonate  $\delta^{18}O$  ( $\delta^{18}O_c$ ) and  $\delta^{13}C$  values of **HU-027** using K-means and Partitioning Around Medioids (PAM) clustering routines (see Supplement S5 in the Zenodo repository). The K-means routine groups datapoints in the  $\delta^{18}O_{c^-}\delta^{13}C$  space into clusters minimizing the squared Euclidian distance between the points within a cluster using the iterative Hartigan-Wong algorithm coded in the "kmeans" function of the "stats" package in R (Hartigan and Wong, 1979; R Core Team, 2023; "stats package," 2019). Clustering was repeated on the same dataset using the PAM algorithm (Kaufman and Rousseeuw, 1990) using the "pam"

398 function of the "cluster" package ("cluster package," 2023; Maechler et al., 2023).

Because of the strong seasonal cycles in productivity, dissolved inorganic carbon composition, freshwater influx and temperature in shallow marine settings, summer and winter seasons are typically recorded through distinct combined  $\delta^{18}O_c$  and  $\delta^{13}C$  signatures in mollusc shells (De Winter et al., 2018; McConnaughey and Gillikin, 2008; Surge et al., 2001). By combining the statistical clustering approach on  $\delta^{18}$ O $_c$  and  $\delta^{13}$ C data with this knowledge of typical seasonal isotopic signatures, we verified the assignment of summer and winter seasons in the geochemical record of HU-027 independent from their sampling location. Note that the assignment of bins in our clumped isotope dataset does not rely on this clustering outcome, as the binning was based primarily on location in the shell and only cross-checked with the statistical clustering.

We modelled the relationship between  $\delta^{18}O_c$ ,  $\delta^{18}O_w$  and clumped isotope-based temperature in the Saiwan environment from the data in specimen HU-027. To do so, we used the relative timing of the four clumped isotope clusters (RB 1 directly preceding R 8 - R 11 and RB 2 preceding and partly overlapping with R 1 - R 7; see Figure 2) and the assumption that the warmest and coldest clusters record summer and winter temperatures, respectively, to determine the order of the clumped isotope clusters throughout the year. We then simulated the pathways between consecutive clusters in the  $\delta^{18}O_c$ ,  $\delta^{18}O_w$  and temperature through a Monte Carlo simulation, taking into account the uncertainty on these three parameters within the clusters. We simulated 1000 linear pathways between the clusters consisting of 100 steps while preserving the relationships between  $\delta^{18}O_{c}$ ,  $\delta^{18}O_{w}$  and temperature, sampling the start and end points from the uncertainty distributions of the parameters in the clusters.

We then estimated  $\delta^{18}O_w$  values for each stable isotope measurement in our compilation for which no clumped isotope values were available using this seasonal  $\delta^{18}O_c$ - $\delta^{18}O_w$  relationship. Since the cyclical nature of the seasonal  $\delta^{18}O_c$ - $\delta^{18}O_w$  relationship produces non-unique  $\delta^{18}O_w$  estimates for any given  $\delta^{18}O_c$  value (see section 3.4), we used the seasonal timing of the  $\delta^{18}O_c$  datapoints to obtain the most likely  $\delta^{18}O_w$  outcome:  $\delta^{18}O_c$  values associated with the warm, high- $\delta^{18}O_w$  spring/summer season (before the summer  $\delta^{18}O_c$  minimum) were assigned the highest of the two possible  $\delta^{18}O_w$  outcomes. Samples associated with the lower temperature and  $\delta^{18}O_w$  half of the seasonal cycle (after the summer  $\delta^{18}O_c$  minimum) were assigned the lowest of the two possible  $\delta^{18}O_w$  outcomes. For the specimens of V vesiculosus (B6) and O. figari (B11), which exhibit higher  $\delta^{18}O_c$  values than the T sanchezi specimens,  $\delta^{18}O_w$  values were assigned based on the seasonal timing of the  $\delta^{18}O_c$  values. Temperatures were calculated for all  $\delta^{18}O_c$  outcomes in our compilation based on the  $\delta^{18}O_c$  measurements and  $\delta^{18}O_w$  estimates. We produce monthly temperature and  $\delta^{18}O_w$  estimates for each specimen by grouping the data obtained from applying the clumped isotope-derived  $\delta^{18}O_c$ - $\delta^{18}O_w$ -temperature relationship on  $\delta^{18}O_c$  profiles in monthly bins per specimen.

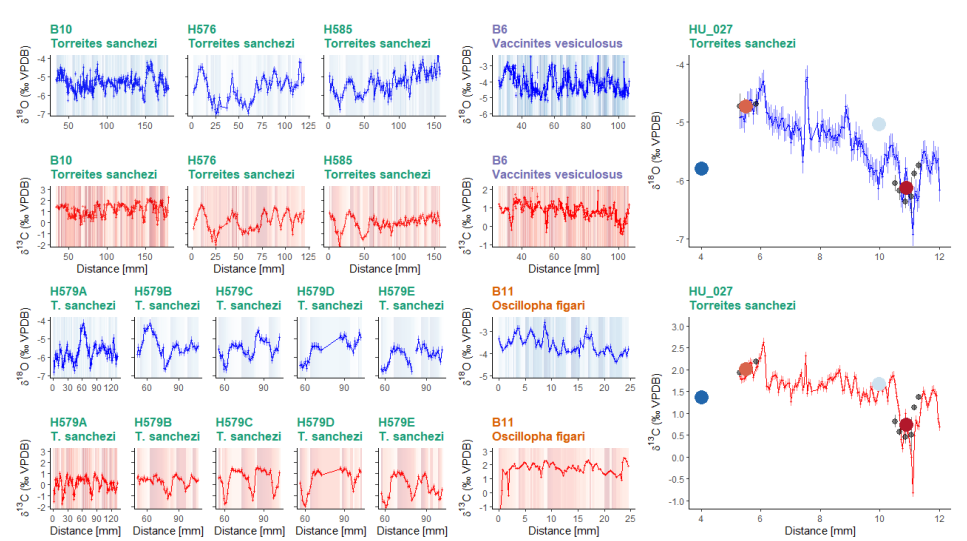
To test the sensitivity of our  $\delta^{18}O_w$  and temperature estimates to the observation that the  $\delta^{18}O_w$  varies seasonally following the **HU-027** clumped isotope outcomes, we also calculated temperatures for all  $\delta^{18}O_c$  profiles using a constant  $\delta^{18}O_w$  value equal to the mean  $\delta^{18}O_w$  value of the three warmer clusters identified in the clumped isotope dataset from **HU-027** (average: -0.25 ‰VSMOW), excluding the cluster that has a low (-4.61  $\pm$  0.86 ‰VSMOW)  $\delta^{18}O_w$  value. We repeated this test assuming the classical (and seasonally constant)  $\delta^{18}O_w$  value of -1 ‰ VSMOW, which is often thought to represent fully marine conditions in a land ice-free climate (Shackleton, 1986). We discuss the impact of the decision not to consider seasonal variability in  $\delta^{18}O_w$  values for these specimens in **section 4.3.** 

## 3. Results

## 3.1 Stable isotope results

All specimens show distinct periodic patterns in  $\delta^{18}O_c$  and  $\delta^{13}C$  values when plotted in growth direction through the shells (**Figure 4**). Stable oxygen isotope values ( $\delta^{18}O_c$ ) in the shells vary between -7.1 %-VPDB and -1.5 %-VPDB with a mean  $\delta^{18}O_c$  value of -5.1  $\pm$  0.9 %-VPDB (1 $\sigma$ ) for the entire dataset. The lowest mean  $\delta^{18}O_c$  values are recorded in *T. sanchezi* shells (-5.5  $\pm$  0.6 %-VPDB; 1 $\sigma$ ), with higher values recorded in *V. vesiculosus* (-4.1  $\pm$  0.6 %-VPDB; 1 $\sigma$ ) and *O. figari* (-3.6  $\pm$  0.4 %-VPDB; 1 $\sigma$ ). Similarly, the lowest mean  $\delta^{13}$ C values are recorded in *T. sanchezi* (0.7  $\pm$  0.9 %-VPDB; 1 $\sigma$ ), followed by *V. vesiculosus* (0.8  $\pm$  0.4 %-VPDB; 1 $\sigma$ ) and *O. figari* (1.7  $\pm$  0.6 %-VPDB; 1 $\sigma$ ).

**Figure 4**: Overview of  $\frac{119}{1}$  incrementally sampled stable oxygen ( $\delta^{18}O_c$ ; blue) and carbon isotope ( $\delta^{13}C_c$ );



red) profiles: 9 profiles through 5 T. sanchezi specimens, of which 5 parallel profiles through specimen H579 (A, B, C, D & F; green frame), and one profile of both  $\delta^{18}$ Q<sub>c</sub> and  $\delta^{13}$ C through V. vesiculosus specimen B6 (E; blue-purple frame) and one profile through O. figari specimen B11 (G; red-orange frame). Vertical axes of T. sanchezi profiles in A-D are equal, while V. vesiculosus, V. figari and V. sanchezi specimen HU-027 have different vertical axes. Records in V represent parallel profiles through the same specimen (H579). The shaded background colours represent time of year based on the ShellChron chronologies constructed using these V sand V

## 3.2 Trace element results

Trace element analyses highlight that shells of all three species are generally characterized by low concentrations of Mn and Fe (**Figure 5**). *T. sanchezi* exhibits median Mn concentrations of 38  $\mu$ g/g (average: 50 ± 44  $\mu$ g/g, 1 $\sigma$ ) and median Fe concentrations of 56  $\mu$ g/g (average: 77 ± 116  $\mu$ g/g, 1 $\sigma$ ) with a

few isolated locations in the shell with concentrations exceeding 300  $\mu$ g/g and 1000  $\mu$ g/g for Mn and Fe, respectively. The carbonate in *V. vesiculosus* has somewhat higher median Mn concentrations of 176  $\mu$ g/g (average: 192  $\pm$  94  $\mu$ g/g, 1 $\sigma$ ) and median Fe concentrations of 125  $\mu$ g/g (average: 173  $\pm$  152  $\mu$ g/g, 1 $\sigma$ ) with some locations showing Mn and Fe concentrations exceeding 500  $\mu$ g/g and 800  $\mu$ g/g, respectively. A clear positive trend is observed towards higher Mn and Fe concentrations in *V. vesiculosus* samples (**Fig. 5A**). Finally, *O. figari* has median Mn concentrations of 63  $\mu$ g/g (average: 75  $\pm$  33  $\mu$ g/g, 1 $\sigma$ ) and much lower median Fe concentrations of 4  $\mu$ g/g (average: 5.7  $\pm$  5.8  $\mu$ g/g, 1 $\sigma$ ), with maximum Mn and Fe concentrations of 180  $\mu$ g/g and 40  $\mu$ g/g, respectively, in some locations.

Mg/Ca and Sr/Ca ratios are very similar between T. sanchezi and V. vesiculosus, with mean Mg/Ca ratios of  $11.4 \pm 2.4$  mmol/mol ( $1\sigma$ ) for T. sanchezi and  $11.5 \pm 4.8$  mmol/mol ( $1\sigma$ ) for V. vesiculosus and mean Sr/Ca ratios of  $1.49 \pm 0.21$  mmol/mol ( $1\sigma$ ) for T. sanchezi and  $1.09 \pm 0.45$  mmol/mol ( $1\sigma$ ) for V. vesiculosus. A subset of the samples from V. vesiculosus exhibit a clear trend towards lower Mg/Ca and Sr/Ca values. O. figari exhibits much lower Mg/Ca values ( $1.87 \pm 1.15$  mmol/mol;  $1\sigma$ ) and Sr/Ca values of  $1.36 \pm 0.18$  mmol/mol ( $1\sigma$ ).

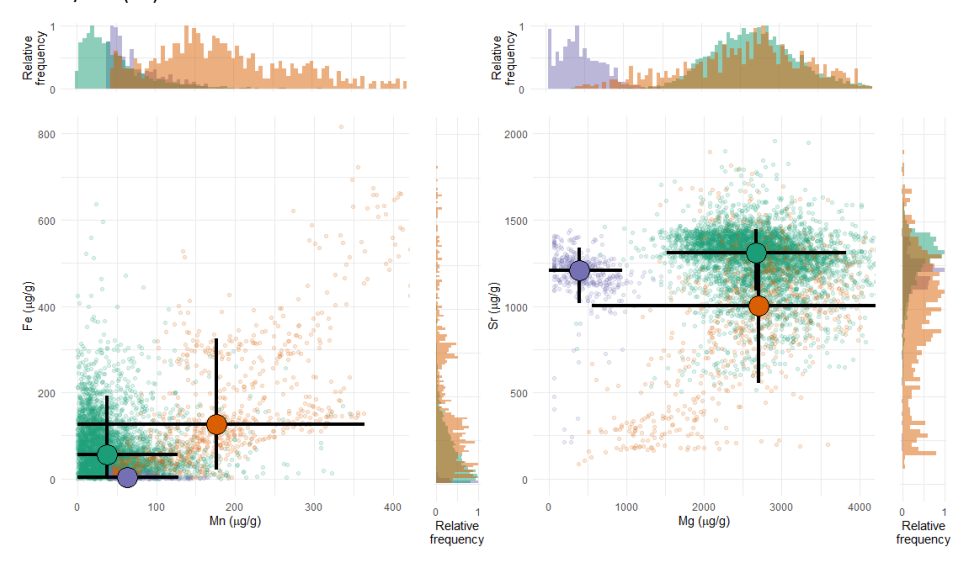


**Figure 5:** Cross plots of manganese vs iron (**A**) and magnesium vs strontium (**B**) concentrations in *T. sanchezi* (green), *V. vesiculosus* (bluepurple) and *O. figari* (redorange) measured using micro-XRF line scan analysis. Shaded points highlight individual measurements in profiles through the shells while bold black crossed lines highlight median concentration values with 2 standard deviations of the variability per species. Histograms on the edges of the plot show the distribution of concentration values in the dataset per element.

# 3.3 Age model results

Applying ShellChron on Mg/Ca, Sr/Ca (only for specimen **B10**),  $\delta^{18}O_c$  and  $\delta^{13}C$  values through all specimens except **HU-037** yielded information about the age-distance relationship in the direction of growth through the shells (**Figure 6**). These distances in growth direction on cross—sections through the shells were

interpreted as proxies for the growth rate of the individual during its life. ShellChron-based age models yield highly consistent age-distance relationships for different *T. sanchezi* specimens, regardless of whether they are based on Mg/Ca, Sr/Ca,  $\delta^{18}$ O<sub>c</sub> or  $\delta^{13}$ C records (**Figure 6A**). Contrarily, growth models based on  $\delta^{18}$ O<sub>c</sub> and  $\delta^{13}$ C values in *V. vesiculosus* and *O. figari* differed (**Figure 6B-C**).

Applying the Daydacna algorithm to trace element records through *T. sanchezi* specimen **B10** (for which subdaily-resolved trace element data is available) yielded independent evidence for the age-depth relationship in shells of *T. sanchezi* (see **Figure 6D**). Except for the Mg/Li record, all age-distance relationships obtained by applying Daydacna on trace element records through specimen **B10** closely agree with the age-distance relationship obtained through the combined ShellChron growth models for this and other *T. sanchezi* specimens. (**Figure 6B**). Of the Daydacna results, the model based on Mg/Li ratios deviates most strongly from the other Daydacna results (based on Mg/Ca, Sr/Ca and Sr/Li records) and the stable isotope-based ShellChron age models. The close agreement between these age models generated using different algorithms, based on different environmental cycles (daily vs seasonal) on different geochemical records through the same specimen, highlights the reproducibility of the age-distance relationship found for our assemblage of *T. sanchezi* specimens from the Saiwan ecosystem. This lends confidence to the interpretation that the observed rhythms in Mg/Ca, Sr/Ca and Sr/Li records in specimen **B10** represent daily cycles (de Winter et al., 2020) and allows us to refine our age model for this species to quantify growth rates on a monthly scale.

Isotope profiles in **Figure 4** and data on the precision of the ShellChron model outcomes in **Table 3** show that the seasonal pattern is in some specimens clearer in  $\delta^{18}O_{c_{\star}}$  while others show clearer seasonality in the  $\delta^{13}C$  records. This translates to a better precision of  $\delta^{18}O_{c^{\star}}$ -based age models in some specimens, while others have better defined better-defined age models based on  $\delta^{13}C$ . On average, the  $\delta^{18}O_{c^{\star}}$ -based age models are more precise (23.1 days at 95% confidence level) than the  $\delta^{13}C$ -based age models (27.6 days at 95% confidence level; see **Table 3**). To account for inter-specimen differences, we decided to use the most precise growth model (either based on  $\delta^{18}O_{c}$  or  $\delta^{13}C$ ) available per specimen for determining the age-distance relationship.

**Table 3**: Median uncertainty (95% CL; in days) of growth models based on  $\delta^{18}O_c$  and  $\delta^{13}C$  profiles through all sequentially sampled specimens. For each specimen, the most precise age model is highlighted in bold.

Specimen	Species	$\delta^{18}O_c$ -based model	$\delta^{13}$ C-based model
		uncertainty (days)	uncertainty (days)
B6	V. vesiculosus	22.9	17.7
B11	O. figari	24.7	57.4
B10	T. sanchezi	22.0	11.3
H576	T. sanchezi	27.7	32.3
H579A	T. sanchezi	18.4	40.4
H579B	T. sanchezi	19.4	39.2
H579C	T. sanchezi	13.4	10.2
H579D	T. sanchezi	32.0	27.2
H579E	T. sanchezi	21.4	9.3
H585	T. sanchezi	29.0	31.0
AVERAGE		23.1	27.6

Formatted: Font: Italic

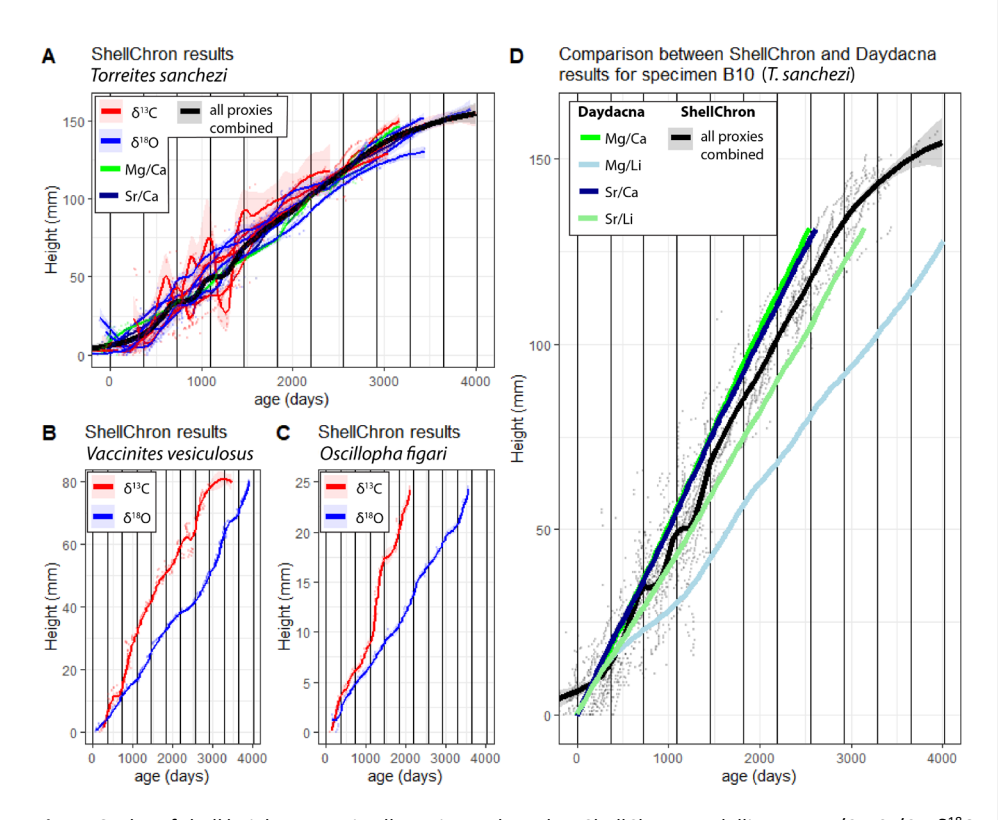


Figure 6: Plot of shell height vs. age in all specimens based on ShellChron modelling on Mg/Ca, Sr/Ca,  $\delta^{18}$ O<sub>c</sub> and  $\delta^{13}$ C profiles in  $\mathit{T. sanchezi}$  (A),  $\delta^{18}$ O<sub>c</sub> and  $\delta^{13}$ C profiles in  $\mathit{V. vesiculosus}$  (B) and  $\delta^{18}$ O<sub>c</sub> and  $\delta^{13}$ C profiles in  $\mathit{O. figari}$  (C). Solid lines represent LOESS smoothed curves (span = 0.2) through the age-height data, with shaded areas indicating uncertainties around the growth models. D) Comparison between ShellChron results for  $\mathit{T. sanchezi}$  specimen B10 profiles (combined chronology from all proxies; black line in panel A) and Daydacna results on subdaily-scale trace element profiles through the same specimen. Colours of curves and uncertainty envelopes represent the proxy on which age modelling was based (see legends in top-left corners of the panels).

## 3.4 Clumped isotope results

Clumped isotope analysis on T. sanchezi specimen HU-027 yielded a mean  $\Delta_{47}$  value of 0.572  $\pm$  0.047 ‰ I-CDES (1 $\sigma$ ). The clusters created from the clumped isotope dataset of specimen HU-027 highlight the relationship between  $\delta^{18}O_c$  values in T. sanchezi and the temperature and  $\delta^{18}O_w$  values reconstructed from clumped isotope thermometry (**Figure 7**). Clustering by location in the shell yields maximum reconstructed temperatures in HU-027 of  $44.2 \pm 4.0$ °C and minimum temperatures of  $19.2 \pm 3.8$ °C. These clusters in sample HU-027 sample a similar or larger spread in  $\delta^{18}O_c$ ,  $\delta^{13}C$  and  $\Delta_{47}$  compared to the statistical clustering approaches that do not take into account the sample location (maximum temperature range:

 $45.4 \pm 17.1^{\circ}$ C to  $24.7 \pm 4.3^{\circ}$ C; see **Supplement S5** in the Zenodo repository), demonstrating that the sampling strategy successfully resolves the seasonal variability recorded in *T. sanchezi* specimen **HU-027**.

Interestingly, while the lowest  $\delta^{18}O_c$  values in  $\it{T. sanchezi}$  are associated with the highest temperatures, as one would expect assuming a constant  $\delta^{18}O_w$  value throughout the year, the highest  $\delta^{18}O_c$  values do not represent the coldest season. This suggests that the Saiwan environment in the Late Campanian experienced significant seasonal variability in  $\delta^{18}O_w$  values. Combining clumped and oxygen isotope data on the clusters shows indeed that they record excursions towards very low  $\delta^{18}O_w$  values (-4.63  $\pm$  0.86 %VSMOW) in the coldest season, far off the  $\delta^{18}O_w$  value of -1 %VSMOW commonly assumed for past greenhouse periods (Shackleton, 1986).

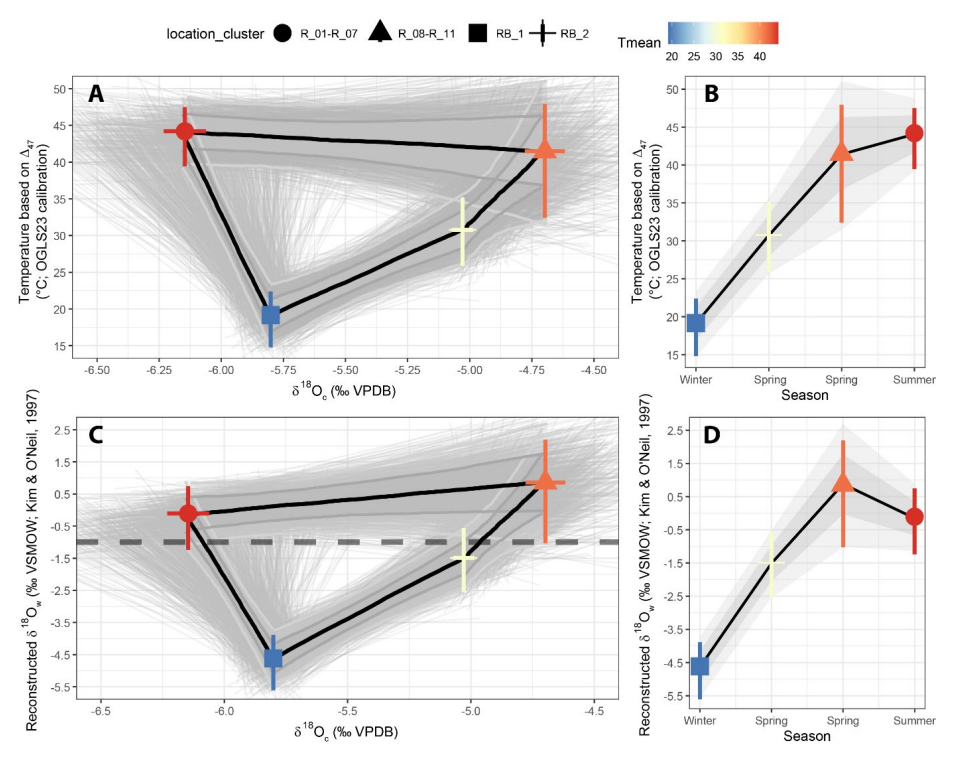


Figure 7: Relationship between temperature and  $\delta^{18}O_c$  values (A) and  $\delta^{18}O_w$  and  $\delta^{18}O_c$  values (C) in  $\mathcal{T}$ . sanchezi shell based on four clusters of clumped isotope analyses through specimen HU-027 grouped by location of the samples in the shell cross\_section (see symbol legend on top). Uncertainties on mean cluster values are reported as 95% confidence levels. The thin black lines and grey shading highlight individual Monte Carlo simulations (N = 1000) of the most likely shape of the  $\delta^{18}O_c$ -temperature and  $\delta^{18}O_c$ - $\delta^{18}O_w$  relationship and their 68% and 95% confidence levels. The horizontal dashed line in B indicates the common assumption of a constant  $\delta^{18}O_w$  value of -1 %-VSMOW throughout the year in the land ice-free Late Cretaceous. Plots B and D show an interpretation of the seasonality in temperature and  $\delta^{18}O_w$  in the Saiwan environment based on these clusters.

## 4. Discussion

#### 4.1 Shell preservation

Ancient shell carbonates, such as the rudists studied here, are known to be susceptible to various forms of diagenetic alteration (Al-Aasm and Veizer, 1986a, 1986b; Brand and Veizer, 1981, 1980; Ullmann and Korte, 2015). Common in carbonate systems, such as the carbonate platforms where the Saiwan rudists were growing, is open-system diagenesis, in which the diagenetic fluid with which the shell carbonate exchanges to alter its chemical and isotopic composition is continuously replaced (Al-Aasm and Veizer, 1986a; Brand and Veizer, 1981). In such systems, the chemical and isotopic composition of carbonates moves away from its original value in an approximately linear trend (mixing line), typically resulting in increased concentrations of trace elements such as Mn and Fe, reduced concentrations of Sr and trends towards lower  $\delta^{18}$ O<sub>c</sub> values in the carbonate (Al-Aasm and Veizer, 1986a, 1986b).

Our detailed geochemical investigation of specimens **B6**, **B10** and **B11** (Figure 2; Figure 5) highlights low Mn and Fe concentrations (typically <300 µg/g and <200 µg/g, respectively, below thresholds used by (Schmitt et al., 2022); see Figure 5) and high Sr concentrations (typically >1.0 mmol/mol; see section 3.2), which show a correlated, skewed distribution tailing towards a few locations on the shell where Mn and Fe concentrations are high and Sr concentrations are low, especially in *V. vesiculosus* specimen **B6** (Figure 5). In *V. vesiculosus*, the trend of covarying elevated Mn and Fe concentrations and coinciding reductions in Mg/Ca and Sr/Ca clearly shows the imprint of local open-system diagenetic remineralization. Open system diagenesis was observed in isolated localities in these fossil shells, which were avoided during sampling for stable and clumped isotope analysis (see section 2.2.3). The chemical differences between well-preserved sections of the shells of these three taxa are likely to reflect taxon-specific variations in trace element concentrations, which are also common in modern molluscs and may reflect differences in shell microstructures and their associated formation pathways (e.g. Carré et al., 2006; Onuma et al., 1979).

Isotopic compositions of carbon and oxygen are often jointly depleted in diagenetically altered materials due to the exchange of shell carbonate with either isotopically depleted meteoric fluids during early diagenetic alteration (Allan and Matthews, 1990) or exchange with pore fluids under high temperatures (e.g. Brand and Veizer, 1981). However, a positive correlation between  $\delta^{18}O_c$  and  $\delta^{18}C$  values is not necessarily a reliable indicator of diagenetic alteration (Swart and Oehlert, 2018). Instead, a positive correlation between  $\delta^{18}O_c$  and  $\delta^{18}C$  values is often observed in modern (non-diagenetically altered) photosymbiotic species, such as tridacnids (Elliot et al., 2009; Killam et al., 2020), and have Such a correlation has been proposed to be caused by seasonal changes in the isotopic composition of the dissolved inorganic carbon pool due to variability in the activity of photosymbionts in phase with the seasonal effect of temperature on the oxygen isotope composition of the shell (Elliot et al., 2009; McConnaughey and Gillikin, 2008). The fact that T. sanchezi specimens in our dataset exhibit a strong positive correlation between  $\delta^{18}O_c$  and  $\delta^{18}C$ , while the other species do not, is corroborated by other evidence that T. sanchezi had photosymbionts such as the presence of specific adaptations in the shell thought to facilitate the hosting of photosymbiotic microorganisms in the mantle and the strong expression of diurnal cycles in shell structure and chemistry (see (N. J. de Winter et al., 2020; Skelton and Wright, 1987; Steuber, 1999)). We therefore disregard this as evidence for open-system diagenesis.

Grain boundary diffusion is another potential diagenetic process that can influence the isotopic composition of biogenic carbonates. This process is rapid on geological timescales (<100 years) and causes the exchange of oxygen isotopes with pore fluids (Adams et al., 2023; Cisneros-Lazaro et al., 2022;

Nooitgedacht et al., 2021). In foraminifera, this process exchanges up to ~3% of the oxygen in the biomineral (Adams et al., 2023), meaning that even in the presence of strongly isotopically negative pore fluids this process can only change the  $\delta^{18}O_c$  value of the biomineral by a few tens of a permille, not enough to fully explain the high temperatures recorded in the fossils in this study.

Finally, our clumped isotope analysis results of specimen **HU-027** may be susceptible to solid statesolid state reordering of the clumped isotope signature, a form of closed-system diagenesis which occurs at elevated temperatures (>100 °C; Chen et al., 2019; Looser et al., 2023; Passey and Henkes, 2012; Stolper and Eiler, 2015). This reordering effect requires large differences between the temperatures in which the carbonate was originally precipitated and the temperatures of the surrounding rocks and, when activated, is likely to affect the entire sample equally rapidly (on geological timescales; Henkes et al., 2014; Stolper and Eiler, 2015). Similarly, heating carbonate samples to 175°C caused a resetting of the  $\Delta_{47}$  value through exchange with internal waters without noticeable change to  $\delta^{18}O_c$  values (Nooitgedacht et al., 2021). Given the fact that significant temperature variability is recorded by the clumped isotope dataset from specimen **HU-027**, and that the recorded temperatures are far from the temperatures needed for the solid-state reordering process to significantly affect isotopic clumping (>100 °C; Henkes et al., 2014), we feel confident in interpreting the recorded temperatures in terms of the paleoclimate and -environment at the Saiwan site.

## 4.2 Seasonality in temperature and $\delta^{18}O_w$ value in Saiwan

The Monte Carlo simulations of the seasonal  $\delta^{18}O_c$ - $\delta^{18}O_w$ -temperature path based on the clumped isotope dataset from specimen HU-027 in Figure 7 show a statistically significant difference between paleotemperatures and  $\delta^{18}O_w$  values between two parts of the annual cycle, especially for the middle range of the  $\delta^{18}O_c$  values of ( $\delta^{18}O_c$  between -5.0 and -6.0 %VPDB). Shell increments deposited after the  $\delta^{18}O_c$  minimum record lower temperature and  $\delta^{18}O_w$  values, while parts of the shell before the  $\delta^{18}O_c$ minimum record high temperature and  $\delta^{18}O_w$  values. High temperatures are reconstructed for both the extreme ends of the  $\delta^{18}O_c$  variability ( $\delta^{18}O_c$  < -6.0 and  $\delta^{18}O_c$  > -5.0 %VPDB). We interpret this as the signature of a shift in the temperature and  $\delta^{18}O_w$  maxima with respect to the  $\delta^{18}O_c$  cycle, with a high temperature extreme (44.2  $\pm$  4.0°C) at the low end of the  $\delta^{18}O_c$  cycle, which we interpret as a hot and dry summer season, and a milder temperature maximum (41.4  $\pm$  4.8°C) at the high end of the  $\delta^{18}O_c$  cycle, which we interpret as a warm and dry spring season (Figure 7B & D). The coldest and wettest season (winter) has such a low  $\delta^{18}$ O<sub>w</sub> value (-4.64  $\pm$  0.86 % VSMOW) that it is not represented by the highest  $\delta^{18}$ O<sub>c</sub> values, as would be the case if  $\delta^{18}$ O<sub>c</sub> would reflect a pure temperature signal (**Figure 7B & D**). This interpretation of the seasonality in Saiwan is also consistent with the temporal relationship between the clumped isotope sampling locations in specimen HU-027: Sample RB 1 (winter) comes earliest in the chronology, closely followed by samples R\_8 - R\_11 (spring), and RB\_2 (spring) directly precedes R\_1 -R\_7 (summer). The latter two partly overlap later in the chronology (Figure 2). The result is a seasonality in which the temperature cycle and the hydrological cycle (reconstructed through the  $\delta^{18}$ O<sub>w</sub> value) are out of phase. The  $\delta^{18}O_c$  value of carbonate precipitated under these conditions therefore exhibits hysteresis behaviour (see Figure 7). Based on the clumped isotope dataset from specimen HU-027 alone, we reconstruct a seasonal sea surface temperature at Saiwan of 19.2 ± 3.8°C to 44.2 ± 4.0°C. The oxygen isotopic composition of the seawater varied from -4.62 ± 0.86 % VSMOW in winter to +0.86 ± 1.6 % VSMOW in summer during the lifetime of specimen **HU-027**.

## 4.3 Monthly temperature, $\delta^{18}O_w$ and growth rate at Saiwan

638 While the strong seasonal variability in  $\delta^{18}O_w$  value of the seawater in Saiwan contradicts the typical 639 explanation of  $\delta^{18}O_c$  fluctuations in mollusc shells, the assumptions under which the ShellChron model 640 operates (see **section 2.4.1**) are not violated by this observation. We believe our characterization of 641 seasonal variability in temperature and  $\delta^{18}O_w$  value to be realistic for the following reasons:

Firstly, this temperature distribution over the year, which is offset in phase from the precipitation seasonality, is observed in modern tropical climates, especially those affected by monsoon-like precipitation seasonality.

Secondly, regardless of the  $\delta^{18}O_c$ -temperature relationship, our clumped isotope data <u>shows-show</u> that the maximum temperature is still recorded by the minimum  $\delta^{18}O_c$  value. Therefore, the combination of  $\delta^{18}O_c$  measurements and seasonal timing based on ShellChron or Daydacna will still assign the correct temperature,  $\delta^{18}O_w$  and growth rates to  $\delta^{18}O_c$  samples in each part of the year. The nonlinear  $\delta^{18}O_c$ -temperature relationship (**Figure 7**) therefore does not undermine the growth rate-temperature discussion.

Thirdly, the comparison between results from the Daydacna algorithm (which is independent from the isotope measurements) with our ShellChron results in specimen **B10** shows the same age for this specimen using both independent methods. If ShellChron would under- or overestimate the age of our specimens due to the nonlinear  $\delta^{18}O_c$ -temperature relationship, this would cause a mismatch between these results.

Finally, a previous study carried out on **B10** (de Winter et al., 2020) presents an analysis of the daily layers in specimen **B10** using multiple lines of evidence. The result of this study is that this specimen records on average 372 daily layers per  $\delta^{18}O_c$  cycle, consistent with astrophysical models of the slow-down of the axial rotation of Earth by friction in the Earth-Moon system, which influences the length of day on geological timescales. The hypothesis that  $\delta^{18}O_c$  cyclicity in *T. sanchezi* represents the full annual cycle (based on ShellChron results) is consistent with this evidence.

Considering the above, we combine information from age models with stable and clumped isotope data from specimen **HU-027** to estimate monthly mean temperature,  $\delta^{18}O_w$  and growth rate for all specimens in the dataset based on their  $\delta^{18}O_c$  values (see **section 2.4.4**). This further data analysis step works under the assumption that the clumped isotope data from specimen **HU-027** samples the seasonal variability in temperature and  $\delta^{18}O_w$  in Saiwan. We also assume that the ShellChron age models based on  $\delta^{18}O_c$  profiles in the other specimens are accurate enough to reliably distinguish between the hot, high- $\delta^{18}O_w$  and cooler low- $\delta^{18}O_w$  half of the annual cycle, such that the correct  $\delta^{18}O_w$  value can be estimated for each  $\delta^{18}O_c$  value in the profile and the  $\delta^{18}O_c$  value can be used to estimate paleotemperature at that time of the year. Given the uncertainty of ShellChron age models for the  $\delta^{18}O_c$  profiles in our compilation (~28 days; see **Table 3**), we believe that our age models are accurate enough to do this.

Figure 8 shows the spread in monthly temperature,  $\delta^{18}O_w$  and growth rate averages. Table 4 also highlights the implications of the seasonal variability in  $\delta^{18}O_w$  throughout the year in the Saiwan environment (see Figure 7C-D): Correcting  $\delta^{18}O_c$  values for  $\delta^{18}O_w$  variability in all specimens yields an average coldest month mean temperature (CMMT) of  $18.7 \pm 3.8^{\circ}$ C and a warmest month mean temperature (WMMT) of  $42.6 \pm 4.0^{\circ}$ C for the entire dataset. Mean annual average temperatures were  $33.1 \pm 4.6^{\circ}$ C. The uncertainties on these estimates are propagated from the uncertainties of the lowest and highest temperature cluster clusters in the clumped isotope dataset (see Table 2 and Figure 7).

Using the classical assumption of a seasonally constant  $\delta^{18}O_w$  value of -1 %VSMOW yields a considerably narrower and warmer monthly temperature range (CMMT – WMMT) of 31.8 – 37.6°C. Alternatively, when we exclude the coldest clumped isotope cluster in the **HU-027** dataset, which has a very low  $\delta^{18}O_w$  value of -4.62 ± 0.86 %VSMOW (**Figure 7**), and might therefore be biased by a strong seasonal influx of meteoric water, and assume the mean of the other three clusters (-0.25 %VSMOW) as a constant  $\delta^{18}O_w$  value, the CMMT-WMMT range becomes 35.7 – 41.8°C. Recent studies demonstrated that the assumption of seasonally constant  $\delta^{18}O_w$  values in shallow marine environments often leads to an underestimation of the seasonal temperature range from  $\delta^{18}O_c$  measurements (e.g. de Winter et al., 2021b). We observe the same effect here and therefore use the seasonal temperature reconstructions that take into account seasonal  $\delta^{18}O_w$  variability from our clumped isotope *T. sanchezi* dataset throughout the remainder of the discussion.

**Table 4**: Overview of monthly mean, maximum and minimum estimates of  $\delta^{49}Q_{\circ}$  (in ‰VPDB),  $\delta^{43}C$  (in ‰VPDB), temperature (in °C),  $\delta^{43}C_{\circ}$  (in ‰VSMOW) and growth rate (in μm/day) per specimen. Note that temperature is estimated in three ways to test the sensitivity to different assumptions for the value of  $\delta^{44}C_{\circ}$ . Firstly, by using the  $\delta^{49}C_{\circ}$ -temperature relationship based on clumped isotope clusters in specimen **HU-027** (see **Fig. 7**). Secondly, by assuming the classical ice-free mean ocean value of -1 ‰VSMOW. Thirdly, by using the mean  $\delta^{49}C_{\circ}$ -value based on the heaviest three clumped isotope clusters in specimen **HU-027** (-0.25 ‰VSMOW); see **Fig. 7B**). In each temperature column, results for the different  $\delta^{49}C_{\circ}$  profiles depend on the same assumption of  $\delta^{49}C_{\circ}$ -variability, so these seasonal temperature estimates are not fully independent from each other. Data given for specimen **HU-027** highlights the spread in temperature outcomes between the clusters instead of monthly values.

**Table 4**: Overview of monthly mean, maximum and minimum estimates of  $\delta^{18}O_c$  (in %VPDB),  $\delta^{13}C$  (in %VPDB), temperature (in °C),  $\delta^{18}O_w$  (in %VSMOW) and growth rate (in µm/day) per specimen. Note that temperature is estimated in three ways to test the sensitivity to different assumptions for the value of  $\delta^{18}O_w$ : Firstly, by using the  $\delta^{18}O_w$ -temperature relationship based on clumped isotope clusters in specimen HU-027 (see Fig. 7). Secondly, by assuming the classical ice-free mean ocean value of -1 % $_{\odot}$ VSMOW. Thirdly, by using the mean  $\delta^{18}$ O $_{\odot}$  value based on the heaviest three clumped isotope clusters in specimen HU-027 (-0.25 %VSMOW; see Fig. 7B). In each temperature column, results for the different  $\delta^{18}O_c$  profiles depend on the same assumption of  $\delta^{18}O_w$  variability, so these seasonal temperature estimates are not fully independent from each other. Data given for specimen HU-027 highlights the spread in temperature outcomes between the clusters instead of monthly values.

specimen	profile	species	δ¹ºO (‰ VPDB)			δ <sup>13</sup> C (‰ VPDB)			Temperature (°C; following δ¹8Oc-T relationship from clumped isotope clusters)			Temperature (°C; assuming δ¹8Ow = -1 ‰VSMOW)			Temperature (°C; assuming $\delta^{18}O_w = -0.25$ %VSMOW)			(% recons clum	δ <sup>18</sup> O <sub>w</sub> VSMO  structed  ped iso lusters	d from tope	<b>Growth rate</b> (μm/d)		
			mean	max	min	mean	max	min	mean	max	min	mean	max	min	mean	max	min	mean	max	min	mean	max	min
B10		Torreites sanchezi	-5.37	-5.04	-5.73	1.13	1.51	0.72	31.8	43.1	20.2	35.1	37.1	33.4	39.2	41.2	37.4	-1.69	0.59	-4.33	28	48	10
B11		Oscillopha figari	-3.58	-3.17	-3.89	1.70	2.01	0.99	31.1	33.8	12.5	25.9	27.5	23.9	29.8	31.3	27.7	0.02	0.82	-3.89	35	59	21
B6		Vaccinites vesiculosus	-4.08	-3.44	-4.57	0.81	1.04	0.67	31.6	36.2	12.2	28.4	30.9	25.2	32.3	34.9	29.0	-0.40	0.82	-4.44	55	76	37
H576		Torreites sanchezi	-5.73	-5.25	-6.23	-0.07	0.76	-1.00	32.8	44.2	19.9	37.1	39.8	34.5	41.2	44.0	38.5	-1.87	0.42	-4.40	46	71	23
H579	Α	Torreites sanchezi	-5.92	-5.43	-6.38	-0.23	0.40	-1.28	37.3	45.1	22.7	38.1	40.6	35.5	42.2	44.8	39.5	-1.17	0.28	-3.65	43	80	19
H579	В	Torreites sanchezi	-5.46	-4.99	-6.36	0.16	0.71	-0.87	35.0	44.9	19.9	35.6	40.5	33.1	39.7	44.7	37.1	-1.15	0.62	-4.40	52	83	0
H579	С	Torreites sanchezi	-5.65	-4.91	-6.17	0.26	1.42	-1.19	33.8	44.0	19.9	36.6	39.4	32.7	40.7	43.6	36.7	-1.59	0.53	-4.40	41	116	0
H579	D	Torreites sanchezi	-5.49	-4.81	-5.90	0.49	1.36	-0.78	29.1	43.4	19.9	35.8	38.0	32.2	39.9	42.1	36.2	-2.33	0.49	-4.48	53	122	19
H579	E	Torreites sanchezi	-5.98	-5.54	-6.61	-0.26	0.94	-1.82	35.9	46.3	19.3	38.4	41.8	36.0	42.6	46.1	40.1	-1.55	0.27	-4.57	62	94	4
H579	average	Torreites sanchezi	-5.70	-5.14	-6.28	0.08	0.97	-1.19	34.2	44.7	20.3	36.9	40.0	33.9	41.0	44.3	37.9	-1.56	0.44	-4.30	50	99	8
H585		Torreites sanchezi	-5.42	-4.64	-6.14	-0.21	0.50	-1.23	32.3	43.7	19.8	35.4	39.3	31.3	39.5	43.5	35.3	-1.65	0.82	-4.44	39	60	12
HU-027		Torreites sanchezi	-5.42	-4.70	-6.15	1.45	2.04	0.72	33.9	44.2	19.2	35.4	39.3	31.6	39.5	43.5	35.6	-1.34	0.86	-4.62			
AVERAGE		-5.28	-4.72	-5.83	0.48	1.15	-0.46	33.1	42.6	18.7	34.7	37.6	31.8	38.8	41.8	35.7	-1.34	0.59	-4.33	45	81	15	

specimen	profile	species	δ¹8O (‰ VPDB)		δ¹³C (‰ VPDB)			Temperature (°C; following δ¹8Oc-T relationship from clumped isotope clusters)			Temperature (°C; assuming $\delta^{18}O_{w} = -1$ %. VSMOW)			Temperature (°C; assuming $\delta^{18}O_w = -0.25$ %oVSMOW)			(% recons clum	<b>5<sup>18</sup>O</b> w 5VSMO tructed ped iso lusters	d from tope		ate		
			mean	max	min	mean	max	min	mean	max	min	mean	max	min	mean	max	min	mean	max	min	mean	max	min
B10		Torreites sanchezi	-5.37	-5.04	-5.73	1.13	1.51	0.72	31.8	43.1	20.2	35.1	37.1	33.4	39.2	41.2	37.4	-1.69	0.59	-4.33	28	48	10
B11		Oscillopha figari	-3.58	-3.17	-3.89	1.70	2.01	0.99	31.1	33.8	12.5	25.9	27.5	23.9	29.8	31.3	27.7	0.02	0.82	-3.89	35	59	21
B6		Vaccinites vesiculosus	-4.08	-3.44	-4.57	0.81	1.04	0.67	31.6	36.2	12.2	28.4	30.9	25.2	32.3	34.9	29.0	-0.40	0.82	-4.44	55	76	37
H576		Torreites sanchezi	-5.73	-5.25	-6.23	-0.07	0.76	-1.00	32.8	44.2	19.9	37.1	39.8	34.5	41.2	44.0	38.5	-1.87	0.42	-4.40	46	71	23
H579	Α	Torreites sanchezi	-5.92	-5.43	-6.38	-0.23	0.40	-1.28	37.3	45.1	22.7	38.1	40.6	35.5	42.2	44.8	39.5	-1.17	0.28	-3.65	43	80	19
H579	В	Torreites sanchezi	-5.46	-4.99	-6.36	0.16	0.71	-0.87	35.0	44.9	19.9	35.6	40.5	33.1	39.7	44.7	37.1	-1.15	0.62	-4.40	52	83	0
H579	С	Torreites sanchezi	-5.65	-4.91	-6.17	0.26	1.42	-1.19	33.8	44.0	19.9	36.6	39.4	32.7	40.7	43.6	36.7	-1.59	0.53	-4.40	41	116	0
H579	D	Torreites sanchezi	-5.49	-4.81	-5.90	0.49	1.36	-0.78	29.1	43.4	19.9	35.8	38.0	32.2	39.9	42.1	36.2	-2.33	0.49	-4.48	53	122	19
H579	E	Torreites sanchezi	-5.98	-5.54	-6.61	-0.26	0.94	-1.82	35.9	46.3	19.3	38.4	41.8	36.0	42.6	46.1	40.1	-1.55	0.27	-4.57	62	94	4
H579	average	Torreites sanchezi	-5.70	-5.14	-6.28	0.08	0.97	-1.19	34.2	44.7	20.3	36.9	40.0	33.9	41.0	44.3	37.9	-1.56	0.44	-4.30	50	99	8
H585		Torreites sanchezi	-5.42	-4.64	-6.14	-0.21	0.50	-1.23	32.3	43.7	19.8	35.4	39.3	31.3	39.5	43.5	35.3	-1.65	0.82	-4.44	39	60	12
HU-027		Torreites sanchezi	-5.42	-4.70	-6.15	1.45	2.04	0.72	33.9	44.2	19.2	35.4	39.3	31.6	39.5	43.5	35.6	-1.34	0.86	-4.62			
AVERAGE			-5.28	-4.72	-5.83	0.48	1.15	-0.46	33.1	42.6	18.7	34.7	37.6	31.8	38.8	41.8	35.7	-1.34	0.59	-4.33	45	81	15

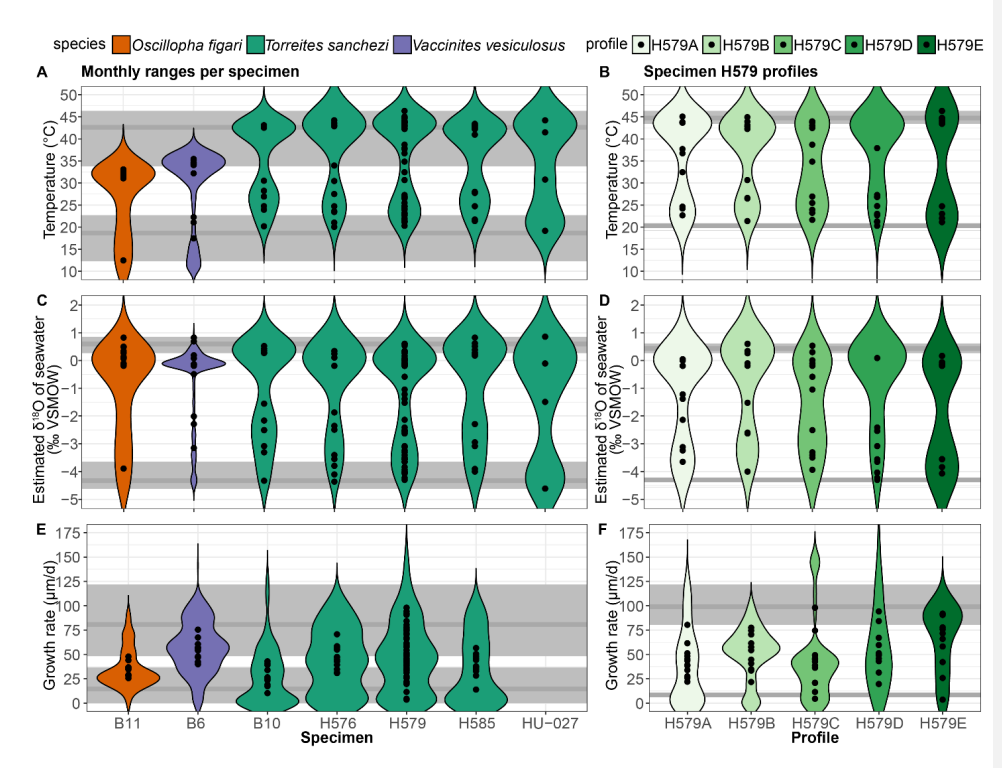


Figure 8: Variability in temperature (A-B), estimated  $\delta^{18}O_w$  (C-D) and growth rate (E-F) in all specimens (A, C & E) and in different profiles of specimen H579 (B, D & E). Coloured violin plots indicate the spread in the full dataset, while black symbols indicate monthly mean values. Grey horizontal lines show the highest and lowest monthly mean value, respectively, through the entire dataset (A, C & E) or specimen H579 (B, D & E) with shaded rectangles indicating variability around these values. Note that growth rates could not be estimated for specimen HU-027, and that the black symbols for this specimen in  $\delta^{18}O_w$  and temperature plots (A and C) indicate values for the four clusters (see Table 1) instead of monthly values.

# 4.4 Inter-species differences

There is a significant difference between the  $\delta^{18}O_c$  ranges recorded in V. vesiculosus, O. figari and T. sanchezi in our dataset (see Figure 8 and Figure 9). When considering the seasonal  $\delta^{18}O_w$  variability in Saiwan, the T. sanchezi specimens record significantly higher temperatures in their shells (19.2 – 45.1 °C range of monthly temperatures, with an average of 33.6°C) than V. vesiculosus (12.2 – 36.2 °C; average: 31.6°C) and V. V0. While the age models allow growth stops, it is possible that some months were not recorded by one or more of these species, reducing the seasonal range. This is also evident from the minimum monthly mean growth rate modelled from some V180 profiles (e.g. in specimen H579; see Table 4) being zero.

Nevertheless, the inter-species difference is surprising, given that these specimens originated from the same biostrome (or directly above, in the case of O. figari; see Figure 1B-C). The lower temperatures (~2 % higher mean  $\delta^{18}O_c$ ) recorded in *O. figari* may be attributed to its slightly higher stratigraphic position. Since the Saiwan site is embedded in a long stratigraphic record and is dated based on ammonite biozones, which yield a dating accuracy on the order of ~100 kyr (Lehmann, 2015), there remains some uncertainty to the (internal) age variability between the units (Kennedy et al., 2000; Schumann, 1995). Therefore, it is possible that the O. figari specimen studied here sampled a different climate and paleoenvironment than the other specimens. This different paleoenvironment may be characterized by a different  $\delta^{18}O_w$  value or seasonal  $\delta^{18}$ O<sub>w</sub> range, resulting in a mild underestimation of paleotemperature and its seasonal range, or a true difference in ambient temperature during the lifetime of the oyster compared to the rudists. Since the mean  $\delta^{18}O_c$  value of O. figari is almost 2 % higher than that of T. sanchezi (**Table 4**), mean annual  $\delta^{18}O_w$ would have to have increased by 2 ‰ within a (geologically) very short time interval, given the close stratigraphic relationship between the species, to explain the difference. A plausible way to achieve such a change might be a shift in the seasonal  $\delta^{18}$ O<sub>w</sub> regime: If the climate in which *O. figari* grew did not feature the highly  $\delta^{18}O_w$ -depleted winter season (see **Figure 7**) and instead featured year-round  $\delta^{18}O_w$  values close to -0.25 %VSMOW (the mean value of the summer and spring/autumn clusters in HU-027), the difference would explain ~1.2 % of the 2 % difference in the  $\delta^{18}O_c$  value. The remaining 0.8 % offset between O. figari and T. sanchezi could then be explained by a drop in mean annual temperature of ~3.5°C over time based on a typical  $\delta^{18}O_c$ -temperature sensitivity of 4.3-4.5 °C/% (Epstein et al., 1953; Grossman and Ku, 1986; Marchitto et al., 2014). In this scenario, the seasonal temperature range experienced by O. figari was roughly 27.7-31.3°C (average temperature of 29.8°C), ~1.3°C lower than the average temperature recorded by O. figari when accounting for the  $\delta^{18}$ O<sub>w</sub> seasonality reconstructed by clumped isotope analysis in specimen HU-027, but with a significantly reduced seasonal variability (Table 4). Note that this constant  $\delta^{18}O_w$  scenario would also significantly increase the estimated winter temperatures from O. figari, which are very low (12.5°C; see **Table 4**) when applying the  $\delta^{18}O_w$  seasonality from our clumped isotope data. We therefore consider it likely that that the strong drop in temperature and  $\delta^{18}O_w$  value that characterized the winter season in Saiwan may not be recorded in O. figari even if it occurred in the climate and environment of O. figari. The temperature distribution in Figure 9D further confirms this by showing that these exceptionally low winter temperatures in O. figari are represented by a small fraction of the data from this specimen, while the majority of the samples record estimated temperatures between 25°C and

726

727

728

729

730

731

732 733

734

735 736

737

738

739 740

741

742

743

744

745

746

747 748

749

750

751

752

753 754

755

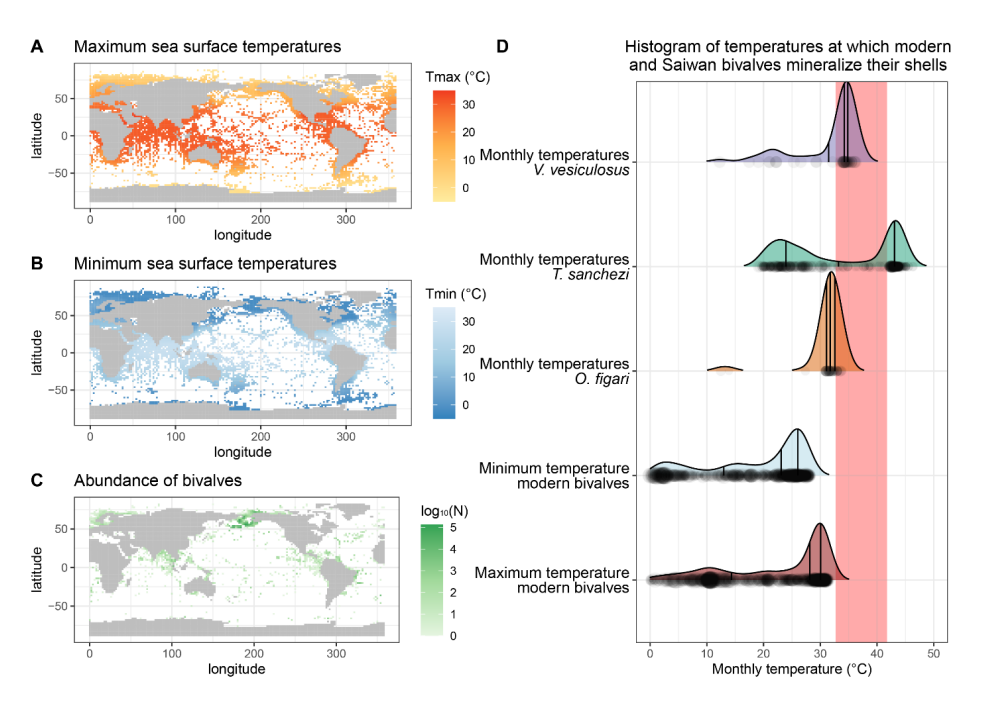


Figure 9: Overview of maximum (A) and minimum (B) modern monthly SST based on the NOAA SST dataset (Huang et al., 2017) at locations of modern bivalve occurrences (C) based on the OBIS dataset (OBIS, 2020) compared with the monthly temperatures reconstructed from the Saiwan fossil molluscs (D). The grey rectangle in (D) marks the range of temperature limits for modern bivalves in the hottest shallow marine environment studied in (Compton et al., 2007): Roebuck Bay.

This stratigraphic argument cannot explain the temperature differences between V. vesiculosus and T. sanchezi, since they were sampled in life position from the same biostrome. Given the rapid growth of these organisms (de Winter et al., 2020; de Winter et al., 2017) and the rapid build-up and succession of the biostromes they are found in (Gili et al., 1995; Gili and Skelton, 2000; Ross and Skelton, 1993), it seems likely that these organisms lived within geologically short time periods from each other (conservatively less than 1000 years), and therefore sampled a similar climate in the Saiwan region. This seems plausible considering the comparatively large overlap in the frequency distribution of temperatures recorded by both species (Table 4; Figure 9D). The growth rate of V. vesiculosus was on average similar to that of T. sanchezi (see Table 4 and Figure 8E) and the spatial sampling resolution in V. vesiculosus (250 µm) was often higher than that in T. sanchezi shells (~100-500 μm (de Winter et al., 2017). Thus, it seems unlikely that the differences between the seasonal ranges obtained from the shells of both species can be attributed to undersampling of the full recorded temperature of V. vesiculosus, a source of variability discussed in (de Winter et al., 2021a; Goodwin et al., 2003; Judd et al., 2017). Applying the high seasonal range in  $\delta^{18}O_w$  observed in **HU-027**, the maximum monthly temperature recorded by *V. vesiculosus* (36.2°C) is at least 5 degrees lower than the maximum monthly temperatures recorded in the T. sanchezi specimens (>43°C in all specimens, average of 44°C; Table 4). At the same time, mean annual temperatures

757 758

759 760

761

762

763

764

765

766

767

768

769 770

771

772

773

774

775

776

777

in *V. vesiculosus* (31.6°C) and *T. sanchezi* (33.0°C) differ by less than 1.5 degrees. As in *O. figari*, winter temperatures in *V. vesiculosus* are exceptionally low compared to temperature ranges in other specimens in the assemblage (**Table 4**) and the temperature distribution in this specimen (**Figure 9D**). This is a consequence of the fact that winter datapoints in the *V. vesiculosus* dataset are associated with the very low  $\delta^{18}O_w$  values reconstructed from the winter datapoints in the clumped isotope dataset, resulting in low temperature estimates when applied on the  $\delta^{18}O_c$  values measured in *V. vesiculosus*. Since all *T. sanchezi* specimens yield consistent winter temperatures of ~20°C, we consider it plausible that *V. vesiculosus* did not record the seasonally low  $\delta^{18}O_w$  conditions and conclude that winter SSTs in Saiwan are more accurately estimated by the *T. sanchezi* data (19-20°C).

The growth rate of *T. sanchezi* specimens is diminished when the range of maximum tolerable temperatures (upper thermal limits) for modern bivalves occurring in hot, shallow marine settings (Roebuck Bay, Australia, tolerable thermal range: 32.7 – 41.8°C; (Compton et al., 2007)) is reached or exceeded (see **Supplement S6** in the Zenodo repository). While the frequency of temperatures recorded by *V. vesiculosus* and *O. figari* specimens in our dataset decreases when these maximum tolerable temperatures are reached (**Figure 109**), temperatures recorded in *T. sanchezi* specimens regularly exceed modern temperature maxima. Higher temperatures recorded in *T. sanchezi* specimens suggest that the upper thermal tolerance of this species may exceed those recorded in modern bivalves and that *T. sanchezi* had a higher temperature tolerance than *V. vesiculosus* and *O. figari*.

This conclusion is further supported by the observation that almost all studied T. sanchezi specimens record a monthly temperature range that exceeds that of V. vesiculosus (and O. figari; Table 4) and that the monthly temperature range recorded by T. sanchezi specimens is consistent (see Figure 8B and Table 4). The fact that all T. sanchezi specimens together record over 30 years of seasonality with consistently low summer  $\delta^{18}O_c$  values (monthly minima of -5.7 %VPDB or lower, corresponding to maximum monthly temperatures >40°C; see Figure 3 & Table 4) also shows that these conditions were not isolated events but a persistent feature of the local climate in Saiwan during the Campanian. Finally, daily rhythms in the shell chemistry of the large T. sanchezi specimen B11 have previously revealed that this specimen likely grew year-round, and thus recorded the full seasonal temperature cycle (de Winter et al., 2020).

An important limitation to this inter-species paleoclimate comparison is that, while the  $\delta^{18}O_c$  profiles presented here record independent records of seasonal variability in different specimens, the interpretation of this  $\delta^{18}O_c$  variability in terms of paleotemperature relies on clumped isotope data collected in one specimen (**HU-027**). Our assumption that all rudist specimens occurred in the same biostrome and sampled a highly similar climate allows us to use the seasonal  $\delta^{18}O_w$  structure inferred from the clumped isotope dataset in **HU-027** to obtain temperature seasonality from  $\delta^{18}O_c$  profiles. Therefore, the temperature reconstructions from different  $\delta^{18}O_c$  profiles are not fully independent.

4.5 Campanian temperature extremes compared to modern climates – Implications for temperature tolerance in past shallow marine environments

**Figure 9A-C** presents an overview of the data on the occurrence of modern bivalves from the OBIS dataset (OBIS, 2020) cross-referenced with the monthly temperatures in these modern locations based on NOAA SST data (Huang et al., 2017) for the years 1981-2010. The lowest monthly temperature in environments containing modern bivalve recordings is -1.8°C. The maximum SST of the warmest month recorded in the NOAA dataset at any location in which modern bivalves are reported is 34.1°C. Based on the combination of these datasets, it becomes clear that the Saiwan environment was warmer than any shallow marine

environment that sustains bivalves in the modern world (**Figure 9D**). The range of temperatures experienced by bivalves in the warmest setting studied by (Compton et al., 2007; 32.7 – 41.8 °C) is frequently exceeded in the Saiwan environment, according to the over 4°C higher mean WMMT estimated from our data (42.6 ± 4.0 °C; **Table 4**; **Figure 8A**). The warmest monthly temperatures in the Saiwan environment thus commonly exceed the maximum monthly temperatures in the living environments of modern bivalves, even when we consider the mean warmest monthly temperature for all specimens instead of the monthly extremes recorded by some *T. sanchezi* specimens in our dataset (44°C). When we consider that bivalves are known to stop growing their shell during stressful periods in the year (e.g. winter in most modern bivalves; Ivany (2012) and summer in some hotter climates Buick and Ivany (2004)), it may be possible (though perhaps unlikely) that the seasonal ranges recorded in our specimens from Saiwan underestimate the true seasonal temperature range in this paleo-environment.

Our clumped isotope data corroborates evidence based on stable oxygen isotope profiles through lowlatitude Tethyan rudists (with assumptions of constant seawater  $\delta^{18}$ O<sub>w</sub> value; e.g. ( de Winter et al., 2017; Steuber et al., 2005) that shallow seas in the Cretaceous Tethys Ocean margins warmed up to temperatures unseen in modern climates (Figure 9), but are not unheard of in the fossil record (e.g. Paleocene-Eocene Thermal Maximum tropical mean annual SSTs >40°C; (Aze et al., 2014)). Clumped isotope data from T. sanchezi specimen HU-027 also reveals that assumptions of year-round constant  $\delta^{18}O_w$  value can be very far off from the true  $\delta^{18}O_w$  seasonality: In the Saiwan site, the coldest season recorded in **HU-027** is characterized by a mean  $\delta^{18}O_w$  value of -4.62  $\pm$  0.86 %VSMOW, which is more than 5% lighter than the mean  $\delta^{18}$ O<sub>w</sub> value during the warmest season (0.86 ± 1.61 %VSMOW). If  $\delta^{18}$ O<sub>w</sub> would be considered constant year-round (e.g. -1 %VSMOW),  $\delta^{18}O_c$ -based temperature reconstructions would underestimate the true seasonality at this site during the Campanian by over 10°C (see discussion in section 4.3 and results in Table 4). Our data instead shows that the low-latitude Saiwan paleoenvironment experienced a higher seasonal temperature range than the roughly contemporary (78 Ma) higher midlatitudes of the Campanian boreal chalk sea recorded in shells from the Kristianstad basin (18.7  $\pm$  3.8 - $42.6 \pm 4.0$  °C, or  $23.9 \pm 6.4$  °C seasonal range for Saiwan vs  $15.3 \pm 4.8 - 26.6 \pm 5.4$  °C, or  $11.2 \pm 7.3$  °C seasonal range for Kristianstad basin), for which seasonal clumped isotope reconstructions were previously presented (de Winter et al., 2021b).

Note that the absolute mean annual temperature for the Saiwan ecosystem (33.1  $\pm$  4.6°C) was significantly higher than that of the higher latitude Boreal Chalk sea (20.1  $\pm$  1.3°C; de Winter et al. (2021b)), yielding a temperature gradient of ~13°C over the latitudes 3°S-50°N. The present-day mean annual sea surface temperatures at the closest weather stations to these localities are 8.2°C (Kristianstad, Sweden, 56°N (de Winter et al., 2021b; Huang et al., 2017)) and 27.9°C (Muscat, Oman, 23°N; (World Sea Temperatures, 2024)), yielding a present-day SST gradient of ~19°C, more than 1.5x that for the same locations in the Campanian. This result corroborates previous evidence from data and models that the latitudinal temperature gradient was smaller compared to the present-day during periods of warmer climate, such as the Campanian (Amiot et al., 2004; Burgener et al., 2018). However, it must be noticed that the paleolatitudes of these sites are slightly different than their modern latitudes.

The Campanian climate in Saiwan is significantly different from that of present-day Oman, which experiences a sea surface temperature seasonality of  $24.2 \pm 1.6 - 31.5 \pm 1.6$ °C (World Sea Temperatures, 2024) and <u>a</u> very limited seasonal precipitation range (0 – 11 mm/month; (climate-data.org, 2024)). The seasonal pattern in temperature and seawater composition in the Campanian is likely caused by large seasonal variability in precipitation, which is common in present-day tropical climates. In this climate,

seasons with hot and relatively dry conditions (summers) are interchanged with cooler seasons featuring an influx of isotopically light water, which diluted the shallow seawater at Saiwan or produced a layer of lower salinity waters close to the sea surface, which was recorded by these very shallow-dwelling photosymbiotic rudists.

The above-mentioned conditions make summers in the Saiwan paleoenvironment hot, even for the Campanian with its global mean annual temperature of 20-25°C (O'Brien et al., 2017). The fact that T. sanchezi apparently thrived under these conditions while V. vesiculosus and O. figari stopped producing their shell at temperatures close to those that limit modern shallow marine bivalves (~34°C; Clarke (2014); Compton et al. (2007)) and perhaps also during the high-precipitation and lower-salinity phases of the winter season. This suggests that T. sanchezi may have been particularly well-adapted to the high seasonality in temperature and precipitation and hot summers in its environment. This hypothesis is further supported by the observation that the genus Torreites occurs exclusively in the late Cretaceous low latitudes  $(18^\circ N - 29^\circ N)$  of the near East and middle America (Global Biodiversity Information Facility, 2024). The unexpectedly high seasonal temperature variability in the Saiwan paleoenvironment  $(18.7 \pm 3.8 - 42.6 \pm 4.0 \,^{\circ}\text{C}$ ; Table 4; Figure 8) might have provided relief for the Saiwan molluscs, since they were not forced to complete their entire life cycle at exceptionally high temperatures and may have recovered from heat exposure during the cooler seasons.

While the conditions in Campanian Saiwan approach the limits of what has been observed for present-day eukaryotes (Clarke, 2014), recent growth experiments on modern gastropods show that temperatures up to 45°C can be tolerated by molluscs for limited amounts of time (Prayudi et al., 2024). Organisms that need to withstand these stressful heat conditions often develop specialized proteins and enzymes to continue bodily functions while experiencing close to lethal temperatures (Tehei et al., 2005; Tehei and Zaccai, 2007). While the Campanian fossils studied here do not preserve remnants of these organic molecules, it is probable that these molluscs employed these molluscs probably employed similar strategies to survive through the extreme summer heat. We thus hypothesize that the members of the Saiwan ecosystem (especially T. sanchezi) must have been evolutionarily adapted to its seasonally hot environment. These observations raise the question whether, given enough time, multicellular organisms such as shallow marine bivalves may survive life in hotter climates, and to which degree the thermal tolerance of modern relatives can be used as a reference point for interpreting the fossil record. More research into extreme paleo-communities such as the Saiwan ecosystem is crucial for understanding the evolutionary limits to which metazoans can adapt to warmer climates, how much time is needed to make these adaptations, and whether such adaptation can come in time to save modern shallow marine communities from rapid climate change.

## Acknowledgements

The authors would like to acknowledge the assistance of Leonard Bik with sample preparation. Arnold van Dijk and Desmond Eefting assisted with the stable isotope analyses in the Utrecht University lab. Stijn van Malderen is acknowledged for his assistance with the LA-ICP-MS measurements. This study has benefitted from discussions with Barbora Krizova, Barbara Goudsmit-Harzevoort, Jingjing Guo and Tobas Agterhuis during data processing of the clumped isotope results and from discussions with Pim Kaskes about the calibration and interpretation of micro-XRF results.

PC acknowledges funding from the Flemish Research Council (FWO; grant nr. G038022N). PC and SG also thank FWO for the financial support for the VUB XRF platform, as well as the VUB Strategic Program for lab maintenance. PC and SG acknowledge funding from the Flemish Research Council (FWO; grant nr. G038022N) for financial support for the VUB XRF platform, as well as the VUB Strategic Research Program. NF was supported by a DAAD fellowship during her stay in the Netherlands and received funding from the EU Erasmus program to fund her lab visit. NJW is supported by an NWO VENI grant (grant nr.: VI.Veni.222.354) and chemical analyses carried out during this project were financially supported by an FWO junior postdoc grant (grant nr. 12ZB220N) and MSCA Individual Fellowship (UNBIAS; 843011) both awarded to NJW. *Torreites sanchezi* specimen HU-27 (BSc-thesis N. al-Fudhaili) was examined with micro-Raman spectroscopy at the University of Padova and we would like to acknowledge the help of Claudio Mazzoli, further Bryan Shirley at University of Erlangen (FAU-GZN) helped with EDS-mapping. HU-27 stable isotopes were kindly measured at FAU-GZN by Daniele Lutz and Michael Joachimski.

## Data availability

905

906

907

908 909

910

911

912913

914

915

916

917 918

919

920

921

922

923

924 925

926

927

All chemical data and annotated Python (for the Daydacna routine) and R (for the remaining workflow) scripts used to carry out the data processing for this study are available in Supplement S7 to this publication as well as through the open-access repository Zenodo (https://doi.org/10.5281/zenodo.12567712). Information about access to specimens H576, H579 and H585 is provided in (Steuber, 1999). Specimens B10 and B11 are archived in the Natural History Museum of Maastricht (the Netherlands), and specimen B6 is archived in the Oertijdmuseum in Boxtel (the Netherlands). Specimen HU-027 is archived at Geozentrum NordBayern at the Friedrich-Alexander Universität in Erlangen (Germany) and the material can be accessed by contacting Matthias López Correa (matthias.lopez@fau.de) or Axel Munnecke (axel.munnecke@fau.de).

## References

- Adams, A., Daval, D., Baumgartner, L.P., Bernard, S., Vennemann, T., Cisneros-Lazaro, D., Stolarski, J.,
   Baronnet, A., Grauby, O., Guo, J., Meibom, A., 2023. Rapid grain boundary diffusion in foraminifera
   tests biases paleotemperature records. Commun Earth Environ 4, 1–11.
   https://doi.org/10.1038/s43247-023-00798-2
  - Al-Aasm, I.S., Veizer, J., 1986a. Diagenetic stabilization of aragonite and low-Mg calcite, II. Stable isotopes in rudists. Journal of Sedimentary Research 56, 763–770.
  - Al-Aasm, I.S., Veizer, J., 1986b. Diagenetic Stabilization of Aragonite and Low-mg Calcite, I. Trace Elements in Rudists. Journal of Sedimentary Research 56.
  - Allan, J.R., Matthews, R.K., 1990. Isotope Signatures Associated with Early Meteoric Diagenesis, in: Carbonate Diagenesis. John Wiley & Sons, Ltd, pp. 197–217. https://doi.org/10.1002/9781444304510.ch16
  - Amiot, R., Lécuyer, C., Buffetaut, E., Fluteau, F., Legendre, S., Martineau, F., 2004. Latitudinal temperature gradient during the Cretaceous Upper Campanian–Middle Maastrichtian: δ18O record of continental vertebrates. Earth and Planetary Science Letters 226, 255–272.
  - Arndt, I., Coenen, D., Evans, D., Renema, W., Müller, W., 2023. Quantifying Sub-Seasonal Growth Rate Changes in Fossil Giant Clams Using Wavelet Transformation of Daily Mg/Ca Cycles. Geochemistry, Geophysics, Geosystems 24, e2023GC010992. https://doi.org/10.1029/2023GC010992
  - Aze, T., Pearson, P.N., Dickson, A.J., Badger, M.P.S., Bown, P.R., Pancost, R.D., Gibbs, S.J., Huber, B.T., Leng, M.J., Coe, A.L., Cohen, A.S., Foster, G.L., 2014. Extreme warming of tropical waters during the Paleocene–Eocene Thermal Maximum. Geology 42, 739–742. https://doi.org/10.1130/G35637.1
  - Batenburg, S.J., Reichart, G.-J., Jilbert, T., Janse, M., Wesselingh, F.P., Renema, W., 2011. Interannual climate variability in the Miocene: High resolution trace element and stable isotope ratios in giant clams. Palaeogeography, Palaeoclimatology, Palaeoecology 306, 75–81.
  - Bernasconi, S.M., Daëron, M., Bergmann, K.D., Bonifacie, M., Meckler, A.N., Affek, H.P., Anderson, N., Bajnai, D., Barkan, E., Beverly, E., Blamart, D., Burgener, L., Calmels, D., Chaduteau, C., Clog, M., Davidheiser-Kroll, B., Davies, A., Dux, F., Eiler, J., Elliott, B., Fetrow, A.C., Fiebig, J., Goldberg, S., Hermoso, M., Huntington, K.W., Hyland, E., Ingalls, M., Jaggi, M., John, C.M., Jost, A.B., Katz, S., Kelson, J., Kluge, T., Kocken, I.J., Laskar, A., Leutert, T.J., Liang, D., Lucarelli, J., Mackey, T.J., Mangenot, X., Meinicke, N., Modestou, S.E., Müller, I.A., Murray, S., Neary, A., Packard, N., Passey, B.H., Pelletier, E., Petersen, S., Piasecki, A., Schauer, A., Snell, K.E., Swart, P.K., Tripati, A., Upadhyay, D., Vennemann, T., Winkelstern, I., Yarian, D., Yoshida, N., Zhang, N., Ziegler, M., 2021. InterCarb: A Community Effort to Improve Interlaboratory Standardization of the Carbonate Clumped Isotope Thermometer Using Carbonate Standards. Geochemistry, Geophysics, Geosystems 22, e2020GC009588. https://doi.org/10.1029/2020GC009588
  - Bernasconi, S.M., Müller, I.A., Bergmann, K.D., Breitenbach, S.F., Fernandez, A., Hodell, D.A., Jaggi, M., Meckler, A.N., Millan, I., Ziegler, M., 2018. Reducing uncertainties in carbonate clumped isotope analysis through consistent carbonate-based standardization. Geochemistry, Geophysics, Geosystems 19, 2895–2914.
  - Brand, U., Veizer, J., 1981. Chemical diagenesis of a multicomponent carbonate system-2: stable isotopes. Journal of Sedimentary Research 51, 987–997.
- Brand, U., Veizer, J., 1980. Chemical diagenesis of a multicomponent carbonate system–1: Trace elements.
   Journal of Sedimentary Research 50.
- Buick, D.P., Ivany, L.C., 2004. 100 years in the dark: Extreme longevity of Eocene bivalves from Antarctica.
   Geology 32, 921–924. https://doi.org/10.1130/G20796.1
- 973 Burgener, L., Hyland, E., Huntington, K.W., Kelson, J.R., Sewall, J.O., 2018. Revisiting the equable climate 974 problem during the Late Cretaceous greenhouse using paleosol carbonate clumped isotope

- 975 temperatures from the Campanian of the Western Interior Basin, USA. Palaeogeography, 976 Palaeoclimatology, Palaeoecology 516, 244–267. https://doi.org/10.1016/j.palaeo.2018.12.004
  - Burke, K.D., Williams, J.W., Chandler, M.A., Haywood, A.M., Lunt, D.J., Otto-Bliesner, B.L., 2018. Pliocene and Eocene provide best analogs for near-future climates. PNAS 115, 13288–13293. https://doi.org/10.1073/pnas.1809600115
    - Carré, M., Bentaleb, I., Bruguier, O., Ordinola, E., Barrett, N.T., Fontugne, M., 2006. Calcification rate influence on trace element concentrations in aragonitic bivalve shells: Evidences and mechanisms. Geochimica et Cosmochimica Acta 70, 4906–4920. https://doi.org/10.1016/j.gca.2006.07.019
    - Cermeño, P., García-Comas, C., Pohl, A., Williams, S., Benton, M.J., Chaudhary, C., Le Gland, G., Müller, R.D., Ridgwell, A., Vallina, S.M., 2022. Post-extinction recovery of the Phanerozoic oceans and biodiversity hotspots. Nature 607, 507–511. https://doi.org/10.1038/s41586-022-04932-6
    - Chen, S., Ryb, U., Piasecki, A.M., Lloyd, M.K., Baker, M.B., Eiler, J.M., 2019. Mechanism of solid-state clumped isotope reordering in carbonate minerals from aragonite heating experiments. Geochimica et Cosmochimica Acta 258, 156–173. https://doi.org/10.1016/j.gca.2019.05.018
    - Cisneros-Lazaro, D., Adams, A., Guo, J., Bernard, S., Baumgartner, L.P., Daval, D., Baronnet, A., Grauby, O., Vennemann, T., Stolarski, J., Escrig, S., Meibom, A., 2022. Fast and pervasive diagenetic isotope exchange in foraminifera tests is species-dependent. Nat Commun 13, 113. https://doi.org/10.1038/s41467-021-27782-8
    - Clarke, A., 2014. The thermal limits to life on Earth. International Journal of Astrobiology 13, 141–154. https://doi.org/10.1017/S1473550413000438
  - climate-data.org, 2024. Duqm climate [WWW Document]. URL https://en.climate-data.org/asia/oman/al-wusta/duqm-151282/ (accessed 5.24.24).
  - cluster package [WWW Document], 2023. URL https://www.rdocumentation.org/packages/cluster/versions/2.1.6 (accessed 11.27.24).
  - Compton, T.J., Rijkenberg, M.J.A., Drent, J., Piersma, T., 2007. Thermal tolerance ranges and climate variability: A comparison between bivalves from differing climates. Journal of Experimental Marine Biology and Ecology 352, 200–211. https://doi.org/10.1016/j.jembe.2007.07.010
  - Daëron, M., Vermeesch, P., 2023. Omnivariant generalized least squares regression: Theory, geochronological applications, and making the case for reconciled Δ47 calibrations. Chemical Geology 121881. https://doi.org/10.1016/j.chemgeo.2023.121881
  - de Winter, N., Sinnesael, M., Makarona, C., Vansteenberge, S., Claeys, P., 2017. Trace element analyses of carbonates using portable and micro-X-ray fluorescence: Performance and optimization of measurement parameters and strategies. Journal of Analytical Atomic Spectrometry. https://doi.org/10.1039/c6ja00361c
  - De Winter, N., Vinzenz Ullmann, C., Sorenson, A., Thibault, N., Claeys, P., 2018. Inter- and intra-specific variability in shell chemistry of well-preserved bivalve shells from the Early Campanian (Late Cretaceous) Kristianstad Basin in Scania, Sweden. Geophysical Research Abstracts 20, 1.
  - de Winter, N.J., 2021. ShellChron 0.2.8: A new tool for constructing chronologies in accretionary carbonate archives from stable oxygen isotope profiles. Geoscientific Model Development Discussions 1–37. https://doi.org/10.5194/gmd-2020-401
  - de Winter, N.J., Agterhuis, T., Ziegler, M., 2021a. Optimizing sampling strategies in high-resolution paleoclimate records. Climate of the Past 17, 1315–1340. https://doi.org/10.5194/cp-17-1315-2021
- de Winter, N.J., Claeys, P., 2016. Micro X-ray fluorescence (μXRF) line scanning on Cretaceous rudist
   bivalves: A new method for reproducible trace element profiles in bivalve calcite. Sedimentology
   64, 231–251. https://doi.org/10.1111/sed.12299
- de Winter, N.J., Goderis, S., Dehairs, F., Jagt, J.W.M., Fraaije, R.H.B., Van Malderen, S.J.M., Vanhaecke, F., Claeys, P., 2017. Tropical seasonality in the late Campanian (late Cretaceous): Comparison

- between multiproxy records from three bivalve taxa from Oman. Palaeogeography, Palaeoclimatology, Palaeoecology 485, 740–760. https://doi.org/10.1016/j.palaeo.2017.07.031
- de Winter, N. J., Goderis, S., Malderen, S.J.M.V., Sinnesael, M., Vansteenberge, S., Snoeck, C., Belza, J.,
   Vanhaecke, F., Claeys, P., 2020. Subdaily-Scale Chemical Variability in a Torreites Sanchezi Rudist
   Shell: Implications for Rudist Paleobiology and the Cretaceous Day-Night Cycle. Paleoceanography
   and Paleoclimatology 35, e2019PA003723. https://doi.org/10.1029/2019PA003723
  - de Winter, N.J., Müller, I.A., Kocken, I.J., Thibault, N., Ullmann, C.V., Farnsworth, A., Lunt, D.J., Claeys, P., Ziegler, M., 2021b. Absolute seasonal temperature estimates from clumped isotopes in bivalve shells suggest warm and variable greenhouse climate. Commun Earth Environ 2, 1–8. https://doi.org/10.1038/s43247-021-00193-9
  - de Winter, N.J., Tindall, J., Johnson, A.L.A., Goudsmit-Harzevoort, B., Wichern, N., Kaskes, P., Claeys, P., Huygen, F., van Leeuwen, S., Metcalfe, B., Bakker, P., Goolaerts, S., Wesselingh, F., Ziegler, M., 2024. Amplified seasonality in western Europe in a warmer world. Science Advances 10, eadl6717. https://doi.org/10.1126/sciadv.adl6717
- de Winter, Niels J., Vellekoop, J., Clark, A.J., Stassen, P., Speijer, R.P., Claeys, P., 2020. The giant marine gastropod Campanile giganteum (Lamarck, 1804) as a high-resolution archive of seasonality in the Eocene greenhouse world. Geochemistry, Geophysics, Geosystems 21, e2019GC008794. https://doi.org/10.1029/2019GC008794
  - Dowsett, H.J., Foley, K.M., Stoll, D.K., Chandler, M.A., Sohl, L.E., Bentsen, M., Otto-Bliesner, B.L., Bragg, F.J., Chan, W.-L., Contoux, C., Dolan, A.M., Haywood, A.M., Jonas, J.A., Jost, A., Kamae, Y., Lohmann, G., Lunt, D.J., Nisancioglu, K.H., Abe-Ouchi, A., Ramstein, G., Riesselman, C.R., Robinson, M.M., Rosenbloom, N.A., Salzmann, U., Stepanek, C., Strother, S.L., Ueda, H., Yan, Q., Zhang, Z., 2013. Sea Surface Temperature of the mid-Piacenzian Ocean: A Data-Model Comparison. Sci Rep 3, 2013. https://doi.org/10.1038/srep02013
  - Elliot, M., Welsh, K., Chilcott, C., McCulloch, M., Chappell, J., Ayling, B., 2009. Profiles of trace elements and stable isotopes derived from giant long-lived Tridacna gigas bivalves: Potential applications in paleoclimate studies. Palaeogeography, Palaeoclimatology, Palaeoecology 280, 132–142. https://doi.org/10.1016/j.palaeo.2009.06.007
  - Epstein, S., Buchsbaum, R., Lowenstam, H.A., Urey, H.C., 1953. Revised carbonate-water isotopic temperature scale. Geological Society of America Bulletin 64, 1315–1326.
  - Evans, D., Müller, W., Oron, S., Renema, W., 2013. Eocene seasonality and seawater alkaline earth reconstruction using shallow-dwelling large benthic foraminifera. Earth and Planetary Science Letters 381. 104–115.
  - Gili, E., Götz, S., 2018. Treatise Online no. 103: Part N, Volume 2, Chapter 26B: Paleoecology of rudists. 1. https://doi.org/10.17161/to.v0i0.7183
  - Gili, E., Skelton, P.W., 2000. Factors regulating the development of elevator rudist congregations.

    Geological Society, London, Special Publications 178, 109–116.

    https://doi.org/10.1144/GSL.SP.2000.178.01.08
  - Gili, E., Skelton, P.W., Vicens, E., Obrador, A., 1995. Corals to rudists—an environmentally induced assemblage succession. Palaeogeography, Palaeoclimatology, Palaeoecology, Palaeoenvironmental Models for the Benthic Associations of Cretaceous Carbonate Platforms in the Tethyan Realm 119, 127–136. https://doi.org/10.1016/0031-0182(95)00064-X
  - Global Biodiversity Information Facility, 2024. Global Biodiversity Information Facility: Torreites [WWW Document]. URL https://www.gbif.org/species/4591957 (accessed 5.10.24).
- Goodwin, D.H., Schöne, B.R., Dettman, D.L., 2003. Resolution and Fidelity of Oxygen Isotopes as Paleotemperature Proxies in Bivalve Mollusk Shells: Models and Observations. PALAIOS 18, 110–125. https://doi.org/10.1669/0883-1351(2003)18<110:RAFOOI&gt;2.0.CO;2
- 1070 Gradstein, F.M., Ogg, J.G., Schmitz, M.D., Ogg, G.M., 2020. Geologic Time Scale 2020. Elsevier.

- 1071 Grossman, E.L., Ku, T.-L., 1986. Oxygen and carbon isotope fractionation in biogenic aragonite: 1072 temperature effects. Chemical Geology: Isotope Geoscience section 59, 59–74.
- Hartigan, J.A., Wong, M.A., 1979. Algorithm AS 136: A K-Means Clustering Algorithm. Journal of the Royal
   Statistical Society. Series C (Applied Statistics) 28, 100–108. https://doi.org/10.2307/2346830
  - Harzhauser, M., Piller, W.E., Müllegger, S., Grunert, P., Micheels, A., 2011. Changing seasonality patterns in Central Europe from Miocene Climate Optimum to Miocene Climate Transition deduced from the Crassostrea isotope archive. Global and Planetary Change 76, 77–84. https://doi.org/10.1016/j.gloplacha.2010.12.003
  - He, B., Olack, G.A., Colman, A.S., 2012. Pressure baseline correction and high-precision CO2 clumpedisotope (Δ 47) measurements in bellows and micro-volume modes. Rapid Communications in Mass Spectrometry 26, 2837–2853.
  - Henkes, G.A., Passey, B.H., Grossman, E.L., Shenton, B.J., Pérez-Huerta, A., Yancey, T.E., 2014. Temperature limits for preservation of primary calcite clumped isotope paleotemperatures. Geochimica et cosmochimica acta 139, 362–382.
  - Huang, B., Thorne, P.W., Banzon, V.F., Boyer, T., Chepurin, G., Lawrimore, J.H., Menne, M.J., Smith, T.M., Vose, R.S., Zhang, H.-M., 2017. NOAA extended reconstructed sea surface temperature (ERSST), version 5. NOAA National Centers for Environmental Information 30, 25.
  - Huyghe, D., Merle, D., Lartaud, F., Cheype, E., Emmanuel, L., 2012. Middle Lutetian climate in the Paris Basin: implications for a marine hotspot of paleobiodiversity. Facies 58, 587–604.
  - IPCC, 2023. SYNTHESIS REPORT OF THE IPCC SIXTH ASSESSMENT REPORT (AR6). Intergovernmental Panel on Climate Change, Geneva, Switzerland.
  - Ivany, L.C., 2012. Reconstructing paleoseasonality from accretionary skeletal carbonates—challenges and opportunities. The Paleontological Society Papers 18, 133–166.
  - Jones, D.S., 1983. Sclerochronology: reading the record of the molluscan shell: annual growth increments in the shells of bivalve molluscs record marine climatic changes and reveal surprising longevity. American Scientist 71, 384–391.
  - Jones, M.M., Petersen, S.V., Curley, A.N., 2022. A tropically hot mid-Cretaceous North American Western Interior Seaway. Geology 50, 954–958. https://doi.org/10.1130/G49998.1
  - Judd, E.J., Wilkinson, B.H., Ivany, L.C., 2017. The life and time of clams: Derivation of intra-annual growth rates from high-resolution oxygen isotope profiles. Palaeogeography, Palaeoclimatology, Palaeoecology. https://doi.org/10.1016/j.palaeo.2017.09.034
  - Kaufman, L., Rousseeuw, P.J., 1990. Partitioning Around Medoids (Program PAM), in: Finding Groups in Data. John Wiley & Sons, Ltd, pp. 68–125. https://doi.org/10.1002/9780470316801.ch2
  - Kennedy, W.J., Jagt, J.W.M., Hanna, S.S., Schulp, A.S., 2000. Late Campanian ammonites from the Saiwan area (Huqf Desert, Sultanate of Oman). Cretaceous Research 21, 553–562. https://doi.org/10.1006/cres.2000.0217
  - Killam, D., Thomas, R., Al-Najjar, T., Clapham, M., 2020. Interspecific and Intrashell Stable Isotope Variation Among the Red Sea Giant Clams. Geochemistry, Geophysics, Geosystems 21, e2019GC008669. https://doi.org/10.1029/2019GC008669
  - Kim, S.-T., O'Neil, J.R., 1997. Equilibrium and nonequilibrium oxygen isotope effects in synthetic carbonates. Geochimica et Cosmochimica Acta 61, 3461–3475.
- Lehmann, J., 2015. Ammonite Biostratigraphy of the Cretaceous—An Overview, in: Klug, C., Korn, D., De
   Baets, K., Kruta, I., Mapes, R.H. (Eds.), Ammonoid Paleobiology: From Macroevolution to
   Paleogeography. Springer Netherlands, Dordrecht, pp. 403–429. https://doi.org/10.1007/978-94 017-9633-0 15
- Looser, N., Petschnig, P., Hemingway, J.D., Fernandez, A., Morales Grafulha, L., Perez-Huerta, A., Vickers,
   M.L., Price, G.D., Schmidt, M.W., Bernasconi, S.M., 2023. Thermally-induced clumped isotope

1076

1077

1078

1079

1080

1081

1082

1083

1084

1085 1086

1087

1088

1089

1090

1091

1092

1093

1094

1095

1096

1097

1098

1099

1100

1101

1102

1103

1104

1105

1106

1107

1108

1109

1110

- resetting in belemnite and optical calcites: Towards material-specific kinetics. Geochimica et Cosmochimica Acta 350, 1–15. https://doi.org/10.1016/j.gca.2023.03.030
- Maechler, M., original), P.R. (Fortran, original), A.S. (S, original), M.H. (S, Hornik [trl, K., maintenance(1999-1200)), ctb] (port to R., Studer, M., Roudier, P., Gonzalez, J., Kozlowski, K., pam()), E.S. (fastpam options for, Murphy (volume.ellipsoid({d >= 3})), K., 2023. cluster: "Finding Groups in Data":
   Cluster Analysis Extended Rousseeuw et al.
- Marchitto, T.M., Curry, W.B., Lynch-Stieglitz, J., Bryan, S.P., Cobb, K.M., Lund, D.C., 2014. Improved oxygen isotope temperature calibrations for cosmopolitan benthic foraminifera. Geochimica et Cosmochimica Acta 130, 1–11.
  - McConnaughey, T.A., Gillikin, D.P., 2008. Carbon isotopes in mollusk shell carbonates. Geo-Marine Letters 28, 287–299. https://doi.org/10.1007/s00367-008-0116-4
  - Müller, I.A., Fernandez, A., Radke, J., van Dijk, J., Bowen, D., Schwieters, J., Bernasconi, S.M., 2017. Carbonate clumped isotope analyses with the long-integration dual-inlet (LIDI) workflow: scratching at the lower sample weight boundaries: LIDI as key for more precise analyses on much less carbonate material. Rapid Communications in Mass Spectrometry 31, 1057–1066. https://doi.org/10.1002/rcm.7878
  - Nooitgedacht, C.W., van der Lubbe, H.J.L., Ziegler, M., Staudigel, P.T., 2021. Internal Water Facilitates
    Thermal Resetting of Clumped Isotopes in Biogenic Aragonite. Geochemistry, Geophysics,
    Geosystems 22, e2021GC009730. https://doi.org/10.1029/2021GC009730
  - OBIS, 2020. Ocean biodiversity information system.
- 1138 O'Brien, C.L., Robinson, S.A., Pancost, R.D., Sinninghe Damsté, J.S., Schouten, S., Lunt, D.J., Alsenz, H., Bornemann, A., Bottini, C., Brassell, S.C., Farnsworth, A., Forster, A., Huber, B.T., Inglis, G.N., 1139 Jenkyns, H.C., Linnert, C., Littler, K., Markwick, P., McAnena, A., Mutterlose, J., Naafs, B.D.A., 1140 1141 Püttmann, W., Sluijs, A., van Helmond, N.A.G.M., Vellekoop, J., Wagner, T., Wrobel, N.E., 2017. 1142 Cretaceous sea-surface temperature evolution: Constraints from TEX 86 and planktonic 1143 foraminiferal oxygen isotopes. Earth-Science Reviews 224-247. 1144 https://doi.org/10.1016/j.earscirev.2017.07.012
  - O'Hora, H.E., Petersen, S.V., Vellekoop, J., Jones, M.M., Scholz, S.R., 2022. Clumped-isotope-derived climate trends leading up to the end-Cretaceous mass extinction in northwestern Europe. Climate of the Past 18, 1963–1982. https://doi.org/10.5194/cp-18-1963-2022
  - Onuma, N., Masuda, F., Hirano, M., Wada, K., 1979. Crystal structure control on trace element partition in molluscan shell formation. Geochemical Journal 13, 187–189.
  - Passey, B.H., Henkes, G.A., 2012. Carbonate clumped isotope bond reordering and geospeedometry. Earth and Planetary Science Letters 351–352, 223–236. https://doi.org/10.1016/j.epsl.2012.07.021
  - Petersen, S.V., Tabor, C.R., Lohmann, K.C., Poulsen, C.J., Meyer, K.W., Carpenter, S.J., Erickson, J.M., Matsunaga, K.K., Smith, S.Y., Sheldon, N.D., 2016a. Temperature and salinity of the Late Cretaceous western interior seaway. Geology 44, 903–906.
  - Petersen, S.V., Winkelstern, I.Z., Lohmann, K.C., Meyer, K.W., 2016b. The effects of Porapak<sup>TM</sup> trap temperature on δ18O, δ13C, and Δ47 values in preparing samples for clumped isotope analysis. Rapid Communications in Mass Spectrometry 30, 199–208.
  - Philip, J.M., Platel, J.-P., 1995. Stratigraphy and rudist biozonation of the Campanian and the Maastrichtian of Eastern Oman. Revista mexicana de ciencias geológicas 12, 15.
  - Prayudi, S.D., Korin, A., Kaminski, M.A., 2024. Thermal tolerance of intertidal gastropods in the Western Arabian Gulf. Journal of Sea Research 197, 102470. https://doi.org/10.1016/j.seares.2024.102470
  - Price, G.D., Bajnai, D., Fiebig, J., 2020. Carbonate clumped isotope evidence for latitudinal seawater temperature gradients and the oxygen isotope composition of Early Cretaceous seas. Palaeogeography, Palaeoclimatology, Palaeoecology 552, 109777. https://doi.org/10.1016/j.palaeo.2020.109777

1129 1130

1131

11321133

1134

1135

1136

1137

1145

1146

1147

1148

1149

1150

1151

1152

1153

1154

1155

1156

1157

1158 1159

1160

1161

1162

1163

1164

- 1166 Provoost, P., Bosch, S., Appeltans, W., OBIS, 2022. robis: Ocean Biodiversity Information System (OBIS) 1167 Client.
- 1168 R Core Team, 2023. R: A Language and Environment for Statistical Computing. R Foundation for Statistical 1169 Computing, Vienna, Austria.
- 1170 Ross, D.J., Skelton, P.W., 1993. Rudist formations of the Cretaceous: a palaeoecological, sedimentological 1171 and stratigraphical review. Sedimentology review/1 73–91.
- Schmitt, K.E., Huck, S., Krummacker, M., De Winter, N.J., Godet, A., Claeys, P., Heimhofer, U., 2022.
  Radiolitid rudists: an underestimated archive for Cretaceous climate reconstruction? Lethaia 55,
  1–21. https://doi.org/10.18261/let.55.4.4
- Schumann, P.D.D., 1995. Upper cretaceous rudist and stromatoporid associations of Central Oman (Arabian Peninsula). Facies 32, 189–202. https://doi.org/10.1007/BF02536868
- 1177 Shackleton, N.J., 1986. Paleogene stable isotope events. Palaeogeography, Palaeoclimatology, 1178 Palaeoecology 57, 91–102.
- 1179 Skelton, P., 2018. Treatise Online no. 104: Part N, Volume 1, Chapter 26A: Introduction to the Hippuritida 1180 (rudists): Shell structure, anatomy, and evolution. Treatise Online.
  - Skelton, P.W., Wright, V.P., 1987. A Caribbean rudist bivalve in Oman-island-hopping across the Pacific in the Late Cretaceous. Palaeontology 30, 505–529.
- 1183 stats package [WWW Document], 2019. URL 1184 https://www.rdocumentation.org/packages/stats/versions/3.6.2 (accessed 4.30.24).
  - Steuber, T., 1999. Isotopic and chemical intra-shell variations in low-Mg calcite of rudist bivalves (Mollusca-Hippuritacea): disequilibrium fractionations and late Cretaceous seasonality. International Journal of Earth Sciences 88, 551–570.
  - Steuber, T., Rauch, M., Masse, J.-P., Graaf, J., Malkoč, M., 2005. Low-latitude seasonality of Cretaceous temperatures in warm and cold episodes. Nature 437, 1341–1344. https://doi.org/10.1038/nature04096
  - Stolper, D.A., Eiler, J.M., 2015. The kinetics of solid-state isotope-exchange reactions for clumped isotopes:

    A study of inorganic calcites and apatites from natural and experimental samples. American
    Journal of Science 315, 363–411. https://doi.org/10.2475/05.2015.01
    - Sun, Y., Joachimski, M.M., Wignall, P.B., Yan, C., Chen, Y., Jiang, H., Wang, L., Lai, X., 2012. Lethally Hot Temperatures During the Early Triassic Greenhouse. Science 338, 366–370. https://doi.org/10.1126/science.1224126
    - Surge, D., Lohmann, K.C., Dettman, D.L., 2001. Controls on isotopic chemistry of the American oyster, Crassostrea virginica: implications for growth patterns. Palaeogeography, Palaeoclimatology, Palaeoecology 172, 283–296.
  - Swart, P.K., Oehlert, A.M., 2018. Revised interpretations of stable C and O patterns in carbonate rocks resulting from meteoric diagenesis. Sedimentary Geology 364, 14–23. https://doi.org/10.1016/j.sedgeo.2017.12.005
- Tehei, M., Madern, D., Franzetti, B., Zaccai, G., 2005. Neutron Scattering Reveals the Dynamic Basis of
  Protein Adaptation to Extreme Temperature \*. Journal of Biological Chemistry 280, 40974–40979.
  https://doi.org/10.1074/jbc.M508417200

  Tehei, M., Zaccai, G., 2007. Adaptation to high temperatures through macromolecular dynamics by
  - Tehei, M., Zaccai, G., 2007. Adaptation to high temperatures through macromolecular dynamics by neutron scattering. The FEBS Journal 274, 4034–4043. https://doi.org/10.1111/j.1742-4658.2007.05953.x
- 1209 Ullmann, C.V., Korte, C., 2015. Diagenetic alteration in low-Mg calcite from macrofossils: a review.
   1210 Geological Quarterly 59, 3–20, doi: 10.7306/gq.1217. https://doi.org/10.7306/gq.1217
- 1211 Vaes, B., van Hinsbergen, D.J.J., van de Lagemaat, S.H.A., van der Wiel, E., Lom, N., Advokaat, E.L.,
   1212 Boschman, L.M., Gallo, L.C., Greve, A., Guilmette, C., Li, S., Lippert, P.C., Montheil, L., Qayyum, A.,
   1213 Langereis, C.G., 2023. A global apparent polar wander path for the last 320 Ma calculated from

1182

1185

1186

1187

1188

1189

1190

1191

1192

1193

1194

1195

1196

1197

1198

1199

1200

1201

1202

- 1214 site-level paleomagnetic data. Earth-Science Reviews 245, 104547. 1215 https://doi.org/10.1016/j.earscirev.2023.104547
- van Hinsbergen, D.J., de Groot, L.V., van Schaik, S.J., Spakman, W., Bijl, P.K., Sluijs, A., Langereis, C.G.,
   Brinkhuis, H., 2015. A paleolatitude calculator for paleoclimate studies. PloS one 10, e0126946.
  - Vansteenberge, S., de Winter, N.J., Sinnesael, M., Xueqin, Z., Verheyden, S., Claeys, P., 2020. Benchtop μXRF as a tool for speleothem trace elemental analysis: Validation, limitations and application on an Eemian to early Weichselian (125–97 ka) stalagmite from Belgium. Palaeogeography, Palaeoclimatology, Palaeoecology 538, 109460. https://doi.org/10.1016/j.palaeo.2019.109460
  - Vellekoop, J., Kaskes, P., Sinnesael, M., Huygh, J., Déhais, T., Jagt, J.W.M., Speijer, R.P., Claeys, P., 2022. A new age model and chemostratigraphic framework for the Maastrichtian type area (southeastern Netherlands, northeastern Belgium). nos 55, 479–501. https://doi.org/10.1127/nos/2022/0703
  - Walliser, E.O., Schöne, B.R., 2020. Paleoceanography of the Late Cretaceous northwestern Tethys Ocean:

    Seasonal upwelling or steady thermocline? PLOS ONE 15, e0238040.

    https://doi.org/10.1371/journal.pone.0238040
  - Wang, Y., Huang, C., Sun, B., Quan, C., Wu, J., Lin, Z., 2014. Paleo-CO2 variation trends and the Cretaceous greenhouse climate. Earth-Science Reviews 129, 136–147. https://doi.org/10.1016/j.earscirev.2013.11.001
    - Wichern, N.M.A., de Winter, N.J., Johnson, A.L.A., Goolaerts, S., Wesselingh, F., Hamers, M.F., Kaskes, P., Claeys, P., Ziegler, M., 2023. The fossil bivalve *Angulus benedeni benedeni*: a potential seasonally resolved stable-isotope-based climate archive to investigate Pliocene temperatures in the southern North Sea basin. Biogeosciences 20, 2317–2345. https://doi.org/10.5194/bg-20-2317-2023
  - World Sea Temperatures, C.G.S.T.-A.-C., 2024. Muscat Water Temperature [WWW Document]. World Sea Temperatures. URL https://www.seatemperature.org/middle-east/oman/muscat.htm (accessed 5.24.24).
- 1239 World Wildlife Fund, 2020. The Living Planet Report 2020 [WWW Document]. URL 1240 http://stats.livingplanetindex.org/ (accessed 2.19.21).